Title

Ultrashort Echo Time Magnetic Resonance Imaging Techniques: Met and Unmet Needs in Musculoskeletal Imaging.

Journal

Journal of Magnetic Resonance Imaging, 55(6)

Authors

Afsahi, Amir

Ma, Yajun

Jang, Hyungseok

et al.

Publication Date

2022-06-01

DOI

10.1002/jmri.28032

Peer reviewed

Published in final edited form as:

J Magn Reson Imaging. 2022 June ; 55(6): 1597–1612. doi:10.1002/jmri.28032.

Ultrashort Echo Time (UTE) MRI Techniques: Met and Unmet Needs in Musculoskeletal Imaging

Amir Masoud Afsahi, MD[1], **Yajun Ma, PhD**[1], **Hyungseok Jang, PhD**[1], **Saeed Jerban, PhD**[1], **Christine B Chung, MD**[1,2], **Eric Y Chang, MD**[1,2], **Jiang Du, PhD**[1,2,*]

[1]Department of Radiology, University of California, San Diego, CA, USA

[2]Research Service, Veterans Affairs San Diego Healthcare System, San Diego, CA, USA

Abstract

This review paper summarizes recent technical development in ultrashort echo time (UTE) magnetic resonance imaging of musculoskeletal (MSK) tissues with short T2 relaxation times. A series of contrast mechanisms are discussed for high contrast morphological imaging of short T2 MSK tissues including the osteochondral junction, menisci, ligaments, tendons, and bone. Quantitative UTE mapping of T1, T2*, T1ρ, adiabatic T1ρ, magnetization transfer ratio, MT modeling of macromolecular proton fraction, quantitative susceptibility mapping, and water content are also introduced. Met and unmet needs in MSK imaging are discussed.

Keywords

UTE; contrast mechanism; qualitative; quantitative; MSK

Introduction

Historically, injury to articular cartilage was considered the primary initiator of osteoarthritis (OA). However, it has been demonstrated that not all cartilage damage leads to OA (1). More recently, understanding of OA has moved from a cartilage-centered focus to the concept of “whole joint organ” disease (2). This includes damage to menisci, ligaments, tendons, subchondral bone-cartilage interface, and subchondral bone, any of which can have effects on both the initiation and progression of cartilage damage. When one tissue begins to deteriorate, it is likely to affect the structural integrity of others and contribute to failure of the joint as a whole (2–4). Unfortunately, many joint tissues such as the osteochondral junction (OCJ), menisci, ligaments, tendons, and bone have short transverse relaxation times (T2s) of a few milliseconds or less (5). They show little signal with conventional magnetic resonance imaging (MRI) sequences with echo times (TEs) of several milliseconds or longer. The lack of signal means that conventional sequences are often of limited value for detecting early changes in these short-T2 tissues or tissue components.

*Corresponding Author: Jiang Du, jiangdu@ucsd.edu, Phone: (858) 246-2248, Fax: (858) 246-2221, University of California, San Diego, Department of Radiology, 9452 Medical Center Dr., San Diego, CA 92037.

Conflicts of Interests

The authors certify that they have no conflicts of interests.

Ultrashort Echo Time (UTE) MRI

UTE sequences with TEs 100–1000 times shorter than those of conventional sequences can directly image the short-T2 tissues in the musculoskeletal (MSK) system (5). By using half-pulse excitation and radial sampling, TEs down to 8 μs have been achieved with two-dimensional (2D) UTE imaging (5). Three-dimensional (3D) UTE imaging can be achieved by combining short hard pulse excitation and 3D radial or spiral sampling (6,7). These UTE sequences make it possible to directly image short-T2 tissues with signal-to-noise ratios (SNR) and contrast-to-noise ratios (CNR) comparable with those of conventional sequences. However, a short TE is not sufficient for high contrast imaging of short-T2 tissues, which typically have low proton densities. Efficient long-T2 suppression is of critical importance for high contrast imaging of short-T2 tissues (8). Quantitative UTE imaging is also important (9–11). The following review focuses on morphological UTE imaging in part I, quantitative UTE imaging in part II, and challenges and future work in part III.

Part I. Morphological UTE Imaging

1. Dual-Echo UTE with Echo Subtraction

Multi-echo acquisition paired with echo subtraction is effective in suppressing long and medium T2 signals for high contrast imaging of short-T2 components (5,6). Because short-T2 signals decay significantly by the time of the second echo, they are minimally affected by the subtraction. Figure 1 shows a sagittal slice of a fat-saturated 3D knee dataset acquired in 10minutes (6). The free induction decay (FID) image yields high signal from all tissues. By subtracting the echo image acquired at the first fat-water-in-phase TE from the FID image, short-T2 components can be highlighted. The dual-echo UTE subtraction technique can be used to detect cartilaginous endplate (CEP) morphology, including CEP thickening and irregularity (12).

2. UTE with Long-T2 Saturation

In this approach a low-power 90° pulse is used to tip the long-T2 magnetization into the transverse plane followed by gradient dephasing (13,14). The short-T2 magnetization is largely unaffected due to significant transverse relaxation during the 90° pulse. Long rectangular pulses are sensitive to the off-resonance effect. Optimized long-T2 suppression pulses and dual-band pulses have been introduced to avoid T1 selectivity or compromising short-T2 signal levels (14). Figure 2 shows UTE imaging of the knee joint with a total scan time of 20minutes. Improved short-T2 contrast was achieved with the dual-band suppression pulse. The patellar tendon and menisci have much improved contrast. Resonance shifts caused the suppression to fail in the fat (short, thick arrows in Figure 3C). The cartilage has a relatively short T2 and is also suppressed.

3. Adiabatic Inversion Recovery UTE (IR-UTE)

In this approach (Figure 3A), an adiabatic fast passage inversion pulse (Silver-Hoult) is used to invert the longitudinal magnetization of long-T2 water and fat (15–20). The longitudinal magnetizations of long-T2 water and fat are fully inverted, but those of short-T2 tissues

are largely saturated due to fast relaxation during the long adiabatic inversion process. The UTE acquisition starts at an inversion time (TI) for the inverted long-T2 magnetization to approach the null point (Figure 3B), leading to selective detection of short-T2 tissues. Adiabatic inversion pulses are insensitive to B1 and B0 inhomogeneities. IR-UTE is a robust contrast mechanism for high contrast imaging of short-T2 tissues (19). Figures 5C–H show representative IR-UTE and clinical imaging of bone at various sites under 3–5minutes. The IR-UTE sequence can also be used to create high contrast for other short-T2 tissues or tissue components such as the OCJ, menisci, ligaments, and tendons.

4. Dual Adiabatic Inversion Recovery UTE (dual-IR-UTE)

In this approach (Figure 4A), two long adiabatic inversion pulses are employed to invert the longitudinal magnetizations of long-T2 water and fat, respectively (21–23). The UTE acquisition starts at a delay time of TI1, which is necessary for the inverted long-T2 water magnetization to reach the null point, and of TI2, which allows the inverted fat magnetization to reach the null point. An appropriate combination of TI1, TI2, and TR allows simultaneous suppression of long-T2 water and fat signals. Dual-IR-UTE imaging of the OCJ (thin arrows) takes about 6minutes (Figure 4F) (21). OCJ effacement and thickening (thick arrows) are also observed. The OCJ is invisible with conventional sequences, whereas it is visible, though with limited contrast, when imaged with UTE or UTE with fat saturation (Figures 4B–F). The dual-IR-UTE sequence can be slightly modified to a double adiabatic inversion recovery UTE (double-IR-UTE) sequence by employing two identical adiabatic inversion pulses with the same center frequency to invert the longitudinal magnetizations of long-T2 tissues (24). High contrast imaging of bone has been generated with this technique.

5. Adiabatic Inversion Recovery Fat-Saturated UTE (IR-FS-UTE)

Figure 5A shows the IR-FS-UTE contrast mechanism to highlight short-T2 signal with efficient suppression of long-T2 water and fat (25–27). The IR-FS-UTE sequence uses a long adiabatic inversion pulse to invert the longitudinal magnetizations of long-T2 tissues such as the nucleus pulposus (NP) in the spine disc. A chemical shift-based fat saturation module is used to further suppress fat signal. To speed up data acquisition, a train of spokes is used after each IR-FS preparation. Figures 5B–D show conventional and IR-FS-UTE imaging of the lumbar spine of a 38-year-old male patient (27). A small incipient Schmorl's node on the vertebral body superior endplate is seen with further detailed characterization of a preserved thin CEP. As expected, this could not be identified on the clinical sequences. In contrast, the 3D IR-FS-UTE sequence shows excellent depiction of the CEP abnormality in the lumber spine under 10minutes. This result demonstrates the feasibility of the IR-FS-UTE sequence in imaging the CEP of the spine with high contrast, as well as its potential in diagnosing early degenerative changes in the intervertebral disc. The IR-FS-UTE sequence can also be used to depict other short-T2 tissues such as the OCJ, tendons, ligaments, menisci, and bone (25).

6. Short TR Adiabatic Inversion Recovery UTE (STAIR-UTE)

The STAIR-UTE sequence employs the basic 3D IR-UTE data acquisition, but with a short TR and a high flip angle (FA) operated with specific absorption rate (SAR) limits for clinical imaging (Figure 6A) (28–30). The combination of a short TR and short TI is chosen for

robust suppression of long-T2 tissues with different T1 values. The STAIR-UTE sequence is insensitive to B1 and B0 inhomogeneities. Multispoke acquisition per IR preparation allows for time-efficient volumetric imaging of short-T2 tissues. Numerical simulation suggests that efficient long-T2 signal suppression can be achieved with a TR <150ms (28). Shorter TRs provide more effective long-T2 signal suppression, and higher FAs provide more T1 weighting. Figures 6B–E show in vivo imaging of the spine of a 31-year-old volunteer. The 3D STAIR-UTE sequence shows high contrast imaging of cortical and trabecular bone in the lumbar spine under 10minutes.

Direct imaging of trabecular bone is extremely challenging due to high signals from marrow fat. Many other contrast mechanisms, such as echo subtraction (5,6), long-T2 saturation (13,14), and spectral presaturation with inversion recovery (SPIR) (31), may not be able to efficiently suppress signals from marrow fat. The residual fat signal can be much higher than that from trabecular bone. For example, Wurnig et al. proposed to use the SPIR-UTE sequence to image trabecular bone (31) and reported a T2* of 2.42±0.56ms at 3T, which is much longer than the T2* of 0.31±0.01ms for trabecular bone measured with STAIR-UTE (28), or a T2* of ~0.3ms for cortical bone measured with various IR-based UTE techniques (32–34). The much longer T2* suggests that SPIR-UTE imaging of trabecular bone is subject to significant fat signal contamination. Meanwhile, the STAIR-UTE-measured T2* values for trabecular bone are very close to the IR-UTE-measured T2* values for cortical bone, which suggests that marrow fat is nearly completely suppressed, with signals from trabeculae being selectively detected in STAIR-UTE imaging (28).

7. UTE Water/Fat Imaging

In conventional UTE imaging, fat saturation is typically required to improve the contrast for short-T2 tissues. However, chemical shift-based fat saturation becomes problematic when imaging short-T2 tissues because the broad spectral width of these tissues may overlap with that of fat. As a result, the fat saturation pulse may inadvertently saturate the signal from short-T2 tissues either directly, or because of magnetization transfer (MT). The single point Dixon (1p-Dixon) approach has been proposed for rapid fat and water separation without short-T2 signal attenuation (35). This method directly decomposes fat and water components from the complex MR signal after correcting for phase error. The UTE single point Dixon technique utilizes dual-echo UTE data acquisition. The FID acquisition is performed immediately after the RF coil deadtime (e.g., 32μs) followed by acquisition of the second echo, where the TE can be chosen flexibly (36). The fat signal in the UTE image is then estimated and suppressed by applying the 1p-Dixon method to the second echo image. Figure 7 shows the 1p-Dixon-based UTE method for high signal and contrast imaging of the Achilles tendon under 4minutes scan time. The UTE image with conventional fat saturation exhibits much decreased signal intensity in the Achilles tendon.

8. UTE Spectroscopic Imaging (UTESI)

UTESI is a combination of highly undersampled interleaved projection reconstruction with a multi-echo UTE acquisition at progressively increasing TEs (37–39). The projections are divided into multiple groups with the data for each group collected with progressively increasing TEs and interleaved projection angles. The undersampled projections within each

group sparsely cover k-space. A view sharing sliding window reconstruction algorithm is used to reconstruct images at each TE (40), followed by Fourier transformation in the time domain to generate spectroscopic images. Figure 8 shows UTESI of the Achilles tendon, where the fascicular pattern of the tensile tendon is depicted with high spatial resolution and excellent contrast without any streak artifacts under 8minutes.

9. Other UTE Techniques for Morphological Imaging

There are many other UTE type sequences developed in recent years, including the acquisition-weighted stack of spirals (AWSOS) sequence (41), water- and fat-suppressed proton projection MRI (WASPI) (42), sweep imaging with Fourier transformation (SWIFT) (43), pointwise encoding time reduction with radial acquisition (PETRA) (44), and zero echo time (ZTE) imaging (45). The contrast mechanisms described above can be combined with these UTE-type sequences for high contrast imaging of various short-T2 tissues in the MSK system. For example, adiabatic IR-based contrast mechanisms can be combined with ZTE and other UTE type sequences for high contrast imaging of short-T2 tissues. Off-resonance saturation contrast (OSC) is another excellent contrast mechanism for SWIFT, WASPI, ZTE, and PETRA, where it is more difficult to use the echo subtraction approach to create short-T2 contrast (46). In fact, SWIFT-based OSC has been used to create high contrast for the OCJ (47). The application of OSC in WASPI, ZTE, and PETRA remains to be investigated.

Part II. Quantitative UTE Imaging

1. UTE T1 Quantification

Conventional inversion recovery-based T1 quantification techniques are problematic for short-T2 tissues. There may be significant signal decay during the relatively long duration inversion pulses used in clinical MR sequences. Quantification of T1 of short-T2 tissues requires the use of UTE sequences (48–51). Variable repetition time (VTR)- and variable flip angle (VFA)-based methods have been widely used for T1 mapping (52–53), but these methods are sensitive to B1 field inhomogeneity. To overcome this problem, the actual flip angle imaging (AFI) technique, which allows rapid 3D B1 mapping, has been proposed (54). However, the current AFI sequence only works for long-T2 tissues, and cannot be used for mapping the B1 and T1 of short-T2 tissues due to the lack of detectable signal. A new T1 measurement method combining the UTE, AFI, and VTR/VFA techniques (3D UTE-AFI-VTR/VFA) has been proposed to address this challenge (55–57). Figure 9 shows excellent T1 fitting for various knee joint tissues of a 35-year-old volunteer (56). The total scan time was less than 10minutes. The T1 values for long-T2 tissues, such as cartilage and muscle, are largely consistent with the literature (53). The T1 values for short-T2 tissues, such as the menisci, ligaments, and tendons remain to be confirmed.

2. UTE T2* Quantification

Conventional sequences cannot provide accurate T2 or T2* mapping for short-T2 tissues due to the lack of detectable signal. Recent studies suggest that UTE-enhanced T2* (UTE-T2*) mapping can assess collagen structural integrity and degeneration in cartilage and menisci, identify subsurface injuries in menisci, evaluate deep subsurface matrix changes

in cartilage after anterior cruciate ligament (ACL) tears, and detect longitudinal changes in cartilage and menisci after anatomic ACL reconstruction (10,11,58,59). Figure 10 shows the longitudinal analyses of UTE-T2* values in the posterior medial meniscus of a group of patients undergoing anatomic ACL reconstruction with a total scan time of 22minutes (59). UTE-T2* mapping can potentially be used to identify joints that are at risk for rapid degeneration and to monitor the effects of new treatments that delay or prevent the development of OA, although further clinical studies are needed.

Biological tissues frequently contain different water compartments which each have distinct T2 or T2* values. UTE bi-component analysis has been developed to quantify T2* values and the short- and long-T2* fractions of water components in a variety of MSK tissues (60–68). Short T2* values and/or fractions have shown significant correlations with tissue properties, such as cartilage degeneration or bone biomechanics (64,65). More recently, UTE tri-component analysis has been proposed to evaluate both short and long T2* components as well as fat in cortical bone (69), but the inclusion of additional components requires more echo images, a longer scan time, and more complicated modeling. The robustness and clinical significance of bi- and tri-component analysis methods remain to be investigated.

3. UTE T1ρ (UTE-T1ρ) Quantification

T1ρ imaging has been proposed to detect early changes of OA associated with PG depletion (70). Recent studies have demonstrated that T1ρ can detect PG loss in bovine cartilage samples as well as OA patients (71–73). T1ρ imaging techniques based on clinical MR sequences may be limited by the fact that short-T2 tissues show a relatively low signal with sequences utilizing TEs of several milliseconds. UTE-T1ρ techniques have been developed to evaluate PG in short-T2 tissues (Figure 11A) (74–76). Figures 11B–E show magnetization-prepared angle-modulated partitioned k-space spoiled gradient echo snapshots (MAPSS) imaging and UTE-T1ρ imaging of the Achilles tendon and meniscus of a volunteer with scan times under 5minutes (74). The MAPSS sequence provides little signal for the Achilles tendon and meniscus because of its relatively long TE of 3.7ms (73). In contrast, the UTE-T1ρ sequence provides much higher signal for the Achilles tendon with a T1ρ of ~3ms and meniscus with a T1ρ of ~8ms, respectively.

4. UTE Adiabatic T1ρ (UTE-AdiabT1ρ) Quantification

T1ρ imaging is sensitive to the magic angle effect (77,78), which makes the evaluation of tissue degeneration complicated. Recently, trains of adiabatic inversion pulses have been used to generate T1ρ relaxation (termed AdiabT1ρ), which is reportedly less sensitive to the magic angle effect (79,80); however, AdiabT1ρ based on conventional MRI sequences are of limited value for short-T2 tissues due to the lack of detectable signal. UTE-AdiabT1ρ sequences have been developed for magic-angle insensitive T1ρ assessment of both short- and long-T2 tissues (81–84). The UTE-AdiabT1ρ sequence (Figure 12A) employs a train of adiabatic IR pulses to generate T1ρ contrast, followed by multi-spoke UTE data acquisition. Figures 12B–I show 3D UTE-AdiabT1ρ imaging of the knee of a 23-year-old volunteer, with a total scan time of 18minutes for seven spin-locking times (TSLs) and showing both high signal and contrast for all major knee joint tissues. Excellent exponential fitting of the

UTE-AdiabT1ρ images with different TSLs demonstrated an AdiabT1ρ value of 13.7±1.0ms for the quadriceps tendon, 22.5±1.2ms for the PCL, 21.5±1.1ms for the meniscus, and 43.5±5.9ms for the patellar cartilage (81).

5. UTE Magnetization Transfer (UTE-MT) Imaging

MT imaging has been introduced for quantitative evaluation of water and macromolecular proton pools (85). Clinical MT sequences cannot assess short-T2 tissues due to the lack of detectable signal. UTE-MT sequences resolve this limitation and can be used to indirectly evaluate macromolecular protons with extremely short T2* values (~0.01ms). The MT pulse is placed at a frequency offset Δf that is away from the narrower lines of water. This strategically placed MT pulse results in saturation of macromolecular (mainly collagen) protons, which exchange with water protons and lead to a reduction in detectable signal. Springer et al. first employed the 3D UTE-MT sequence to calculate MT ratio (MTR) in cortical bone (86). However, MTR is only semi-quantitative and shows only moderate correlation with tissue properties (87). A two-pool MT model has been proposed to extract fundamental parameters about a free pool composed of water protons and a semisolid pool composed of collagen protons (88). Multiple spokes (N_{sp}) can be acquired after each MT preparation to reduce the scan time by a factor of N_{sp} (89). Figure 13 shows the basic UTE-MT sequence, along with imaging of a bovine cortical bone sample. Excellent two-pool MT modeling and MT parameter mapping were achieved using a Gaussian lineshape. On a related note, MMF derived from UTE-MT modeling seems to be insensitive to the magic angle effect (90), and is highly correlated with biomechanics and degeneration (91–94). As such, the multi-spoke 3D UTE-MT technique has been used to evaluate knee joint degeneration in vivo with a total scan time of less than 15minutes. Decreased MMF and MTR were observed for cartilage and meniscus in mild and advanced OA as compared to healthy subjects (95,96).

6. UTE Quantitative Susceptibility Mapping (UTE-QSM)

QSM has recently emerged as a promising technique that allows characterization of tissue based on its magnetic susceptibility (97). QSM can estimate the spatial susceptibility distribution from a measured field perturbance using nonlinear optimization techniques. Tissue with paramagnetic iron shows elevated susceptibility, which increases with iron concentration. The susceptibility of hemosiderin in the synovium is more challenging to measure with conventional MRI due to high levels of iron with very short T2* values that result in a lack of detectable signal. A 3D UTE-QSM framework has been developed to estimate the magnetic susceptibility of short-T2 tissues including cortical bone and hemosiderin (98–103). Figure 14 shows two UTE-QSM slices from a 28-year-old hemophilia patient who subsequently underwent total knee arthroplasty (TKA), and the corresponding histology images for synovial tissues, namely Tissue A and Tissue B, harvested from two different regions of the knee joint (99). Three dual-echo UTE datasets were acquired under a total scan time of 18minutes. The histology showed densely distributed hemosiderin exhibited by blue dots in Tissue A (Figure 14B), but much lower iron density in Tissue B (Figure 14D). The estimated susceptibility was 4.5±1.8ppm for Tissue A and 2.7±1.1ppm for Tissue B, demonstrating lower susceptibility in Tissue B consistent with histological iron staining.

UTE-QSM can also be used to assess bone mineral density (BMD) in cortical bone. A recent study by Dimov et al. found good correlation between bone CT and QSM values in the porcine hoof (R^2=0.77) (98). Jerban et al. found that 3D UTE-QSM was negatively correlated with μCT-based volumetric BMD (R^2=0.49), and positively correlated with bone porosity (R^2=0.46) in human cortical bone specimens (103).

7. UTE Water Content Quantification

Water content in short-T2 tissues can be quantified by comparing their UTE signal intensities with that of a water phantom. One example is UTE imaging of cortical bone, where both bound and pore water contribute to the UTE signal (49). Total water (bound water plus pore water) can be measured by comparing UTE signal with an external phantom. Mean total bone water concentrations of 17.4±2.2%, 28.7±1.3%, and 41.1±9.6% have been reported for pre- and postmenopausal groups as well as for patients with renal osteodystrophy, respectively (49). Manhard et al. employed the adiabatic inversion recovery (AIR) sequence to map bound water content, and the dual adiabatic full passage (DAFP) sequence to map pore water content in cortical bone (Figure 15) (51). Excellent correlations were observed between bending strength and bound and pore water concentrations. Jerban et al. employed UTE to measure total water content, IR-UTE to measure bound water content, the UTE/IR-UTE difference to calculate pore water content, and UTE-MT modeling to measure collagen backbone proton density (93,94). Furthermore, UTE measures are significantly correlated with bone microstructure and biomechanical properties. For example, collagen proton density is correlated with BMD (R^2=0.50), Young's modulus (R^2=0.37), yield stress (R^2=0.36), and ultimate stress (R^2=0.36). Incomplete long-T2 signal suppression has the potential to affect bound water quantification, but other techniques, such as dual-IR-UTE, double-IR-UTE, and STAIR-UTE sequences may provide more accurate bound water mapping.

8. Other Techniques for Quantitative Imaging

There are many other UTE-type techniques which have been developed for quantitative imaging of short-T2 tissues. For example, the SWIFT sequence can be combined with a variable flip angle approach (VFA-SWIFT) to measure the T1 of short-T2 components in articular cartilage (104). T2* can also be measured using some novel techniques. For example, though the ZTE sequence cannot map T2* based on the traditional variable TE approach, Wiesinger et al. overcame the limitation by proposing a Looping Star pulse sequence based on the radial rotating ultra-fast imaging sequence extended by a time-multiplexed gradient-refocusing mechanism (105). Multiple magnetic coherences are excited and gradient-refocused in the shape of a looping k-space trajectory, allowing the Looping Star technique to capture an initial FID image followed by gradient echo images at equidistant TEs. However, the accuracy and efficiency of the various quantitative UTE-type imaging techniques remain to be investigated.

Part III. Challenges and Future Work

Of the various morphological imaging techniques, adiabatic IR-based approaches, including single IR-UTE (15–20), Dual-IR-UTE (21–23), double-IR-UTE (24), IR-FS-UTE (25–27),

and STAIR-UTE (28–30), appear to provide more uniform suppression of long-T2 water and fat signals. This is attributable to the insensitivity of adiabatic pulses to B1 and B0 inhomogeneities (15–17). Saturation-based approaches, including T2-selective RF excitation (TELEX) (13), WASPI (42), UTE-OSC (46), and dual-band UTE (14), may be more sensitive to B1 and B0 inhomogeneities. Dual-echo UTE with echo subtraction is a simple technique capable of high-contrast imaging of short-T2 tissues (5,6,8,12). However, it is sensitive to B0 inhomogeneity and susceptibility, especially for the later echo (8). Fat separation-based methods, such as the single-point Dixon and UTESI, can be incorporated in UTE imaging (36–38), but they typically require longer acquisition time and data post-processing. A systematic comparison of the various contrast mechanisms and their combination with different UTE type sequences in terms of CNR and SNR efficiencies for different short-T2 tissues remains to be investigated.

Most UTE sequences are developed at 3T, although there are some studies reporting UTE imaging at 1.5T or 7T. Higher field strength, stronger gradients, and dedicated extremity coils are helpful for UTE imaging of short-T2 tissues which typically suffer from low SNR due to relatively low proton densities and fast signal decay (106). UTE imaging at field strength lower than 1.5T remains to be investigated. Generally, UTE type sequences are less sensitive to artifacts such as motion, pulsation, and wraparound due to oversampling of k-space center and elimination of phase encoding (107). However, eddy currents are major factors limiting clinical applications. ZTE is insensitive to eddy currents, and has great potential for clinical studies. For example, there is an increased interest in imaging bone with ZTE sequences (108,109). ZTE allows visualization of cortical bone and intraosseous lesions that are occult at CT (Figure 16). These cysts differed from the subchondral ganglion cysts identified during grading and were confirmed in patients' standard-of-care MRI examinations (108). "CT-like" images can be automatically generated on the scanner. The high-contrast bone images are well suited for 3D volume rendering using commonly employed ray casting algorithms. ZTE with 1.0mm isotropic resolution only requires 3–4minutes of imaging time which is good for clinical applications (109).

While the series of quantitative UTE MR imaging techniques allow mapping of short-T2 tissues' properties and relaxation times, there are several major challenges. The first challenge is long-T2 signal contamination, which leads to significant quantification errors. This is especially the case for T2* mapping of thin structures such as the OCJ and the CEP. As the OCJ is very thin (i.e., 0.1–0.2mm) and curved, T2* derived from regular UTE with variable TEs is likely subject to significant errors due to the partial volume effect (110). The adiabatic IR-based UTE sequences provide efficient long-T2 suppression, and thus much more accurate T2* mapping (23). The second challenge is related to fat contamination and off-resonance artifacts (111). Fat contamination may significantly affect MR relaxation times as well as tissue properties (such as T1, T2*, MMF, QSM, and water content). Furthermore, center-out radial or spiral sampling of k-space in UTE imaging employs a different direction for each readout. Off-resonance artifacts are manifested as blurring due to the ring-shaped point spread function (111). This produces effects that differ from those seen in Cartesian sampling of k-space. Center-out radial artifacts are important to recognize as they can simulate normal structures and disease. The third challenge is the magic angle effect (77–80). The magic angle-associated increase in T1ρ, T2, or T2* can be significantly

higher than the increase caused by degeneration. Magic angle-insensitive techniques such as UTE-AdiabT1ρ (81–84) and UTE-MT modeling of MMF (89–96), are of particular interest for robust assessment of short-T2 tissue degeneration.

Direct imaging of short-T2 tissues can be used to improve diagnosis of OA and other MSK diseases. The widely used MRI scoring method (WORMS) incorporates 14 features, but they are mostly related to articular cartilage (112). Ligaments, tendons, and bone are not included in WORMS. Meniscus is considered but clinical MRI provides little signal for this largely short-T2 tissue. There are no widely accepted imaging scoring systems for menisci, ligaments, and tendons, at least in part due to limited morphological visualization (e.g., little signal, poor contrast) and a lack of sensitivity to small degrees of changes in structural integrity. UTE imaging with high signal, spatial resolution, and contrast for the principal joint tissues will likely improve the classification of disease, which may aid in the development of new grading systems.

A natural next step is to combine morphological and quantitative imaging of both short- and long-T2 tissues in the joint for more comprehensive assessment of degeneration. This follows the concept of “whole joint organ” disease, not only morphologically, but quantitatively. Deep learning-based automatic segmentation and quantitative relaxometry of all major joint tissues will likely facilitate translational study of the novel morphological and quantitative UTE MRI techniques (113–115). Clearly, a significant amount of work remains to be done for robust detection of joint degeneration at the early stages.

Conclusion

In summary, there is significant interest in direct UTE imaging and quantification of short-T2 tissues. Short-T2 contrast can be generated with a variety of techniques including echo subtraction, long-T2 saturation, adiabatic inversion, spectroscopic imaging, and combinations of these techniques. MR properties including T1, T2*, T1ρ, and adiabT1ρ can be measured using UTE techniques combined with the appropriate preparation pulses. Tissue properties, including total, bound and free water content, macromolecular fraction, and susceptibility can also be quantified with a variety of UTE-based techniques. Further research is needed to evaluate the efficiency of each technique, to correlate UTE measures with histopathology and biomechanics, and to investigate their applications in OA and other MSK diseases.

Acknowledgement

The authors acknowledge grant support from NIH (R01AR062581, R01AR068987, R01AR075825, R01AR078877, and R21AR075851), the VA Clinical Science Research & Development Service (1I01CX001388 and I21RX002367), and GE Healthcare.

Reference

1. Meachim G, Emery IH. Quantitative aspects of patello-femoral cartilage fibrillation in Liverpool necropsies. Ann Rheum Dis 1974;33:39–47. [PubMed: 4132379]
2. Hayashi D, Guermazi A, Hunter DJ. OARSI year in review 2010: imaging. Osteoarthritis Cartilage 2011;19:354–360. [PubMed: 21320616]

3. Brandt KD, Radin EL, Dieppe PA, Putte L. Yet more evidence that osteoarthritis is not a cartilage disease (Editorial). Ann Rheum Dis 2006;65:1261–1264. [PubMed: 16973787]
4. Kijowski R, Woods MA, McGuine TA, Wilson JJ, Graf BK, De Smet AA. Arthroscopic Partial Meniscectomy: MR Imaging for Prediction of Outcome in Middle-Aged and Elderly Patients. Radiology 2011;259:203–212. [PubMed: 21330563]
5. Robson MD, Gatehouse PD, Bydder M, Bydder GM. Magnetic resonance: an introduction to ultrashort TE (UTE) imaging. J Comput Assist Tomogr 2003;27:825–846. [PubMed: 14600447]
6. Rahmer J, Bornert P, Groen J, Bos C. Three-dimensional radial ultrashort echo-time imaging with T2 adapted sampling. Magn Reson Med 2006;55:1075–1082. [PubMed: 16538604]
7. Carl M, Bydder GM, Du J. UTE imaging with simultaneous water and fat signal suppression using a time-efficient multi-spoke inversion recovery pulse sequence. Magn Reson Med 2016;76:577–582. [PubMed: 26309221]
8. Du J, Bydder M, Takahashi AM, Carl M, Chung CB, Bydder GM. Short T2 contrast with three-dimensional ultrashort echo time imaging. Magn Reson Imaging 2011;29:470–82. [PubMed: 21440400]
9. Chang E, Du J, Chung C. UTE imaging in the musculoskeletal system. J Magn Reson Imaging 2015;41:870–883. [PubMed: 25045018]
10. Williams A, Qian Y, Bear D, Chu CR. Assessing degeneration of human articular cartilage with ultra-short echo time (UTE) T2* mapping. Osteoarthritis Cartilage 2010;18:539–546. [PubMed: 20170769]
11. Williams A, Qian Y, Golla S, Chu CR. UTE-T2* mapping detects subclinical meniscus injury after anterior cruciate ligament tear. Osteoarthritis Cartilage 2012;20:486–494. [PubMed: 22306000]
12. Kim YJ, Cha JG, Shin YS, et al. 3D ultrashort TE MRI for evaluation of cartilaginous endplate of cervical disk in vivo: feasibility and correction with disk degeneration in T2-weighted spin-echo sequence. AJR 2018;210:1131–1140. [PubMed: 29629793]
13. Sussman MS, Pauly JM, Wright GA. Design of practical T2-selective RF excitation (TELEX) pulses. Magn Reson Med 1998;40:890–899. [PubMed: 9840834]
14. Larson PE, Gurney PT, Nayak K, Gold GE, Pauly JM, Nishimura DG. Designing long-T2 suppression pulses for ultrashort echo time imaging. Magn Reson Med 2006;56:94–103. [PubMed: 16724304]
15. Reichert ILH, Robson MD, Gatehouse PD, et al. Magnetic resonance imaging of cortical bone with ultrashort TE (UTE) pulse sequences. Magn Reson Imaging 2005;23:611–618. [PubMed: 16051035]
16. Larson PE, Conolly SM, Pauly JM, Nishimura DG. Using adiabatic inversion pulses for long-T2 suppression in ultrashort echo time (UTE) imaging. Magn Reson Med 2007;58:952–961. [PubMed: 17969119]
17. Du J, Carl M, Bydder M, Takahashi A, Chung CB, Bydder GM. Qualitative and quantitative ultrashort echo time (UTE) imaging of cortical bone. J Magn Reson 2010;207:304–311. [PubMed: 20980179]
18. Horch R, Gochberg D, Nyman J, Does M. Clinically-compatible MRI strategies for discriminating bound and pore water in cortical bone. Magn Reson Med 2012;68:1774–1784. [PubMed: 22294340]
19. Du J, Bydder GM. Qualitative and quantitative ultrashort-TE MRI of cortical bone. NMR Biomed 2013;26:489–506 [PubMed: 23280581]
20. Ma Y, Fan S, Shao H, et al. Clinical use of multiplied, subtracted and/or fitted inversion recovery (MASTIR) pulse sequences. Quant Imaging Med Surg 2020;10:1334–1369. [PubMed: 32550142]
21. Du J, Takahashi A, Bae WC, Chung CB, Bydder GM. Dual inversion recovery, ultrashort echo time (DIR UTE) imaging: creating high contrast for short-T2 species. Magn Reson Med 2010;63:447–455. [PubMed: 20099332]
22. Bae W, Dwek JR, Znamirowski R, et al. Ultrashort TE MRI of the osteochondral junction of the knee at 3T: Identification of anatomic structures contributing to signal intensity. Radiology 2009;254:837–845.

23. Du J, Carl M, Bae WC, et al. Dual inversion recovery ultrashort echo time (DIR-UTE) imaging and quantification of the zone of calcified cartilage (ZCC). Osteoarthritis Cartilage 2013;21:77–85 [PubMed: 23025927]
24. Ma YJ, Zhu Y, Lu X, Carl M, Chang EY, Du J. Short T2 imaging using a 3D double adiabatic inversion recovery prepared ultrashort echo time cones (3D DIR-UTE-Cones) sequence. Magn Reson Med 2018;79:2555–2563 [PubMed: 28913879]
25. Ma Y, Jerban S, Carl M, et al. Imaging of the region of the osteochondral junction (OCJ) using a 3D adiabatic inversion recovery prepared ultrashort echo time Cones (3D IR-UTE Cones) sequence at 3T. NMR Biomed 2019;32:e4080. [PubMed: 30794338]
26. Wei Z, Lombardi A, Lee R, et al. Comprehensive assessment of in vivo lumbar spine intervertebral discs using a 3D adiabatic T1ρ prepared ultrashort echo time (UTE-Adiab-T1ρ) pulse sequence. Quant Imaging Med Surg 2021;21–308. [PubMed: 33392008]
27. Lombardi A, Wei Z, Wong J, et al. High contrast cartilaginous endplate imaging using a 3D adiabatic inversion-recovery-prepared fat- saturated ultrashort echo time (3D IR-FS-UTE) sequence. NMR Biomed 2021;e4579. [PubMed: 34219287]
28. Ma Y, Chen Y, Li L, et al. Trabecular bone imaging using a 3D adiabatic inversion recovery prepared ultrashort echo time cones sequence at 3T. Magn Reson Med 2020;83:1640–1651. [PubMed: 31631404]
29. Ma Y, Jang H, Wei Z, et al. Myelin imaging in human brain using a short repetition time adiabatic inversion recovery prepared ultrashort echo time (STAIR-UTE) MRI sequence in multiple sclerosis. Radiology 2020;297:392–404. [PubMed: 32779970]
30. Ma Y, Jang H, Wei Z, et al. Brain ultrashort T2 component imaging using a short TR adiabatic inversion recovery prepared dual-echo ultrashort TE sequence with complex echo subtraction (STAIR-dUTE-ES). J Magn Reson 2021;323:106898. [PubMed: 33429170]
31. Wurnig MC, Calcagni M, Kenkel D, et al. Characterization of trabecular bone density with ultra-short echo-time MRI at 1.5, 3.0, and 7.0 T -comparison with micro-computed tomography. NMR Biomed 2014;27:1159–1166. [PubMed: 25088271]
32. Jerban S, Ma Y, Wei Z, Jang H, Chang EY, Du J. Quantitative magnetic resonance imaging of cortical and trabecular bone. Seminars in Musculoskeletal Radiology 2020;24:386–401. [PubMed: 32992367]
33. Jerban S, Lu X, Dorthe EW, et al. Correlation of cortical bone microstructural and mechanical properties with water proton fractions obtained from ultrashort echo time (UTE) MRI tricomponent T2* model. NMR Biomed 2020;e4233. [PubMed: 31820518]
34. Ma Y, Jerban S, Jang H, Chang D, Chang EY, Du J. Quantitative ultrashort echo time (UTE) magnetic resonance imaging of bone: an update. Front Endocrinol 2020;11:567417.
35. Ma J A single-point dixon technique for fat-suppressed fast 3D gradient-echo imaging with a flexible echo time. J Magn Reson Imaging 2008;27:881–890. [PubMed: 18302201]
36. Jang H, Carl M, Ma Y, et al. Fat Suppression for Ultrashort Echo Time Imaging Using a Single Point Dixon Method. NMR Biomed 2019;32:e4069. [PubMed: 30768813]
37. Du J, Hamilton G, Takahashi A, Bydder M, Chung CB. Ultrashort echo time spectroscopic imaging (UTESI) of cortical bone. Magn Reson Med 2007;58(5):1001–9. [PubMed: 17969110]
38. Du J, Takahashi AM, Chung CB. Ultrashort TE spectroscopic imaging (UTESI): application to the imaging of short T2 relaxation tissues in the musculoskeletal system. J. Magn Reson Imaging 2009;29:412–421. [PubMed: 19161197]
39. Du J, Chiang AJ, Chung CB, et al. Orientational analysis of the Achilles tendon and enthesis using an ultrashort echo time spectroscopic imaging sequence. Magn Reson Imaging 2009;28:178–184. [PubMed: 19695811]
40. Du J, Carroll TJ, Brodsky E, et al. Contrast enhanced peripheral magnetic resonance angiography using time-resolved vastly undersampled isotropic projection reconstruction. J Magn Reson Imaging 2004;20:894–900. [PubMed: 15503332]
41. Qian Y, Williams A, Chu CR, Boada FE. High-resolution ultrashort echo time (UTE) imaging on human knee with AWSOS sequence at 3.0T. J Magn Reson Imaging 2012;35:204–210. [PubMed: 22002811]

42. Cao H, Ackerman JL, Hrovat MI, Graham L, Glimcher MJ, Wu Y. Quantitative bone matrix density measurement by water- and fat-suppressed proton projection MRI (WASPI) with polymer calibration phantoms. Magn Reson Med 2008;60:1433–1443. [PubMed: 19025909]
43. Idiyatullin D, Corum C, Park JY, Garwood M. Fast and quiet MRI using a swept radiofrequency. J Magn Reson 2006;181:342–349. [PubMed: 16782371]
44. Grodzki DM, Jakob PM, Heismann B. Ultrashort echo time imaging using pointwise encoding time reduction with radial acquisition (PETRA). Magn Reson Med 2012;67:510–518. [PubMed: 21721039]
45. Weiger M, Pruessmann KP, Hennel F. MRI with zero echo time: hard versus sweep pulse excitation. Magn Reson Med 2011;66: 379–389. [PubMed: 21381099]
46. Du J, Takahashi A, Bydder M, Chung CB, Bydder GM. Ultrashort TE imaging with off-resonance saturation contrast (UTE-OSC). Magn Reson Med 2009;62:527–531. [PubMed: 19449436]
47. Rautiainen J, Salo EN, Tiitu V, et al. Assessment of human tibial cartilage-bone interface in osteoarthritis using SWIFT. In: Proceedings of ISMRM 21st Annual Meeting, Salt Lake City, Utah, USA, 2013.P0434.
48. de Mello R, Ma Y, Ji Y, Du J, Chang EY. Quantitative MRI MSK techniques: an update. AJR 2019;213:524–533. [PubMed: 30995086]
49. Techawiboonwong A, Song HK, Leonard MB, Wehrli FW. Cortical bone water: in vivo quantification with ultrashort echo-time MR imaging. Radiology 2008;248:824–833. [PubMed: 18632530]
50. Chen J, Grawn S, Shao H, D'Lima D, Bydder GM, Du J. Evaluation of bound and pore water in cortical bone using ultrashort echo time (UTE) magnetic resonance imaging. NMR Biomed 2015;28:1754–1762. [PubMed: 26527298]
51. Manhard MK, Uppuganti S, Granke M, Gochberg DF, Nyman JS, Does MD. MRI-derived bound and pore water concentrations as predictors of fracture resistance. Bone 2016;87:1–10. [PubMed: 26993059]
52. Deoni SC, Rutt BK, Peters TM. Rapid combined T_1 and T2 mapping using gradient recalled acquisition in the steady state. Magn Reson Med 2003;49:515–26. [PubMed: 12594755]
53. Gold GE, Han E, Stainsby J, Wright GA, Brittain J, Beaulieu C. Musculoskeletal MRI at 3.0T: relaxation times and image contrast. Am J Neuroradiol 2004;183:343–350.
54. Yarnykh VL. Actual flip-angle imaging in the pulsed steady state: a method for rapid three-dimensional mapping of the transmitted radiofrequency field. Magn Reson Med 2007;57:192–200. [PubMed: 17191242]
55. Ma Y-J, Lu X, Carl M, Zhu Y, Szeverenyi NM, Bydder GM, et al. Accurate T1 mapping of short T2 tissues using a three-dimensional ultrashort echo time cones actual flip angle imaging-variable repetition time (3D UTE-Cones AFI-VTR) method. Magn Reson Med 2018;80:598–608. [PubMed: 29314235]
56. Ma Y-J, Zhao W, Wan L, Guo T, Searleman A, Jang H, et al. Whole knee joint T1 values measured in vivo at 3T by combined 3D ultrashort echo time cones actual flip angle and variable flip angle methods. Magn Reson Med 2019;81:1634–44. [PubMed: 30443925]
57. Wei Z, Ma Y, Jang H, Yang W, Du J. To measure T1 of short T2 species using an inversion recovery prepared three-dimensional ultrashort echo time (3D IR-UTE) method: a phantom study. J Magn Reson 2020;314:106725. [PubMed: 32320926]
58. Williams A, Qian Y, Golla S, Chu CR. UTE-T2* mapping detects subclinical meniscus injury after anterior cruciate ligament tear. Osteoarthritis Cartilage 2012;20:486–494. [PubMed: 22306000]
59. Chu CR, Williams AA, West RV, Qian Y, Fu FH, Do BH, Bruno S. Quantitative magnetic resonance imaging UTE-T2* mapping of cartilage and meniscus healing after anatomic anterior cruciate ligament reconstruction. Am J Sports Med 2014;42:1847–1856. [PubMed: 24812196]
60. Qian Y, Williams A, Chu CR, Boada FE. Multi-component T2* mapping of knee cartilage: technical feasibility ex vivo. Magn Reson Med 2010;64:1426–1431. [PubMed: 20865752]
61. Diaz E, Chung CB, Bae WC, et al. Ultrashort echo time spectroscopic imaging (UTESI): an efficient method for quantifying bound and free water. NMR Biomed 2012;25:161–168. [PubMed: 21766381]

62. Du J, Diaz E, Carl M, Bae W, Chung C, Bydder GM. Ultrashort echo time imaging with bicomponent analysis. Magn Reson Med 2012;67:645–649. [PubMed: 22034242]
63. Biswas R, Bae W, Diaz E, et al. Ultrashort echo time (UTE) imaging with bicomponent analysis: bound and free water evaluation of bovine cortical bone subject to sequential drying. Bone 2012;50:749–755. [PubMed: 22178540]
64. Bae WC, Chen PC, Chung CB, Masuda K, DLima D, Du J. Quantitative ultrashort echo time (UTE) MRI of human cortical bone: correlation with porosity and biomechanical properties. J Bone Miner Res 2012;27:848–857. [PubMed: 22190232]
65. Pauli C, Bae WC, Lee M, et al. Ultrashort echo time (UTE) magnetic resonance imaging of the patella with bi-component analysis: correlation with histopathology and polarized light microscopy. Radiology 2012;264:484–493. [PubMed: 22653187]
66. Shao H, Chang EY, Zanganeh S, et al. UTE bi-component analysis of T2* relaxation in articular cartilage. Osteoarthritis Cartilage 2016;24:364–373. [PubMed: 26382110]
67. Kijowski R, Wilson JJ, Liu F. Bicomponent ultrashort echo time T2* analysis for assessment of patients with patellar tendinopathy. J Magn Reason Imaging 2017;46:1441–1447.
68. Breda SJ, de Vos RJ, Poot DHJ, Krestin GP, Hernandez-Tamames JA, Oei EHG. Association between T2* relaxation times derived from ultrashort echo time MRI and symptoms during exercise therapy for patellar tendinopathy: a large prospective study. J Magn Reason Imaging 2021;54:1596–1605.
69. Lu X, Jerban S, Wan L, et al. Three Dimensional Ultrashort Echo Time Imaging with Tri-component Analysis for Human Cortical Bone. Magn Reson Med 2019;82:348–355. [PubMed: 30847989]
70. Duvvuri U, Reddy R, Patel SD, Kaufman JH, Kneeland JB, Leigh JS. T1rho-relaxation in articular cartilage: effects of enzymatic degradation. Magn Reson Med 1997;38:863–867. [PubMed: 9402184]
71. Regatte RR, Akella SVS, Wheaton AJ, et al. 3D-T1ρ-relaxation mapping of articular cartilage: in vivo assessment of early degenerative changes in symptomatic osteoarthritic subjects. Acad Radiology 2004;11:741–749.
72. Duvvuri U, Kudchodkar SB, Reddy R, Leigh JS. T1ρ relaxation can assess longitudinal proteoglycan loss from articular cartilage in vitro. Osteoarthritis Cartilage 2002;10:838–844. [PubMed: 12435327]
73. Li X, Han ET, Ma B, Busse RF, Majumdar S. In vivo T1ρ mapping in cartilage using 3D magnetization-prepared angle-modulated partitioned k-space spoiled gradient echo snapshots (3D MAPSS). Magn Reson Med 2008;59:298–307. [PubMed: 18228578]
74. Du J, Carl M, Diaz E, et al. Ultrashort TE T1rho (UTE T1rho) Imaging of the Achilles Tendon and Meniscus. Magn Reson Med 2010;64:834–842. [PubMed: 20535810]
75. Du J, Statum S, Znamirowski R, Bydder GM, Chung CB. Ultrashort TE T1rho magic angle imaging. Magn Reson Med 2013;69:682–687. [PubMed: 22539354]
76. Ma YJ, Carl M, Shao H, Tadros AS, Chang EY, Du J. Three-dimensional ultrashort echo time cones T1rho (3D UTE-cones-T1rho) imaging. NMR Biomed 2017;30:3709.
77. Du J, Statum S, Znamirowski R, Bydder GM, Chung CB. Ultrashort TE T1rho magic angle imaging. Magn Reson Med 2013;69:682–687. [PubMed: 22539354]
78. Shao H, Pauli C, Li S, Ma Y, Tadros AS, Kavanaugh A, et al. Magic angle effect plays a major role in both T1rho and T2 relaxation in articular cartilage. Osteoarthritis Cartilage 2017;25:2022–2030. [PubMed: 28161394]
79. Casula V, Nissi MJ, Podlipska J, et al. Elevated adiabatic T1ρ and T2ρ in articular cartilage are associated with cartilage and bone lesions in early osteoarthritis: a preliminary study. J Magn Reson Imaging 2017;46:678–689. [PubMed: 28117922]
80. Hänninen N, Rautiainen J, Rieppo L, Saarakkala S, Nissi MJ. Orientation anisotropy of quantitative MRI relaxation parameters in ordered tissue. Sci Rep 2017;7:9606. [PubMed: 28852032]
81. Ma Y, Carl M, Searleman A, Lu X, Chang EY, Du J. Three dimensional adiabatic T1ρ prepared ultrashort echo time Cones (3D AdiabT1ρ UTE-Cones) sequence for whole knee imaging. Magn Reson Med 2018;80:1429–1439. [PubMed: 29493004]

82. Wu M, Zhao W, Wan L, et al. Quantitative three-dimensional ultrashort echo time cones imaging of the knee joint with motion correction. NMR Biomed 2020;33:e4214. [PubMed: 31713936]
83. Wu M, Ma Y, Wan L, et al. Magic angle effect on adiabatic T1ρ imaging of the Achilles tendon using 3D ultrashort echo time cones trajectory. NMR Biomed 2020;33:e4322. [PubMed: 32431025]
84. Wu M, Ma Y, Kasibhatla A, et al. Convincing Evidence for Magic Angle Less-Sensitive Quantitative T1ρ Imaging of Articular Cartilage Using the 3D Ultrashort Echo Time Cones Adiabatic T1ρ (3D UTE Cones-AdiabT1ρ) Sequence. Magn Reson Med 2020;84:2551–2560. [PubMed: 32419199]
85. Henkelman RM, Huang X, Xiang Q, Stanisz GJ, Swanson SD, Bronskill MJ. Quantitative interpretation of magnetization transfer. Magn Reson Med 1993;29:759–766. [PubMed: 8350718]
86. Springer F, Martirosian P, Machann J, Schwenzer NF, Claussen CD, Schick F. Magnetization transfer contrast imaging in bovine and human cortical bone applying an ultrashort echo time sequence at 3 Tesla. Magn Reson Med 2009;61:1040–1048. [PubMed: 19267348]
87. Chang EY, Bae WC, Shao H, et al. Ultrashort echo time magnetization transfer (UTE-MT) imaging of cortical bone. NMR Biomed 2015;28:873–880. [PubMed: 25981914]
88. Sled JG, Pike GB. Quantitative imaging of magnetization transfer exchange and relaxation properties in vivo using MRI. Magn Reson Med 2001;46:923–31. [PubMed: 11675644]
89. Ma Y, Carl M, Chang EY, Du J. Quantitative Magnetization Transfer Ultrashort Echo Time Imaging Using a Time-Efficient 3D Multispoke Cones Sequence. Magn Reson Med 2018;79:692–700. [PubMed: 28470838]
90. Ma Y, Shao H, Chang EY, Du J. UTE magnetization transfer (UTE-MT) imaging and modeling: magic angle independent biomarkers of tissue properties. NMR Biomed 2016;29:1546–1552. [PubMed: 27599046]
91. Ma Y, Tadros AS, Du J, Chang EY. Quantitative Two-Dimensional Ultrashort Echo Time Magnetization Transfer (2D UTE-MT) Imaging of Cortical Bone. Magn Reson Med 2017;79:1941–1949. [PubMed: 28776754]
92. Zhu Y, Cheng X, Ma Y, et al. Rotator cuff tendon assessment using magic-angle insensitive 3D ultrashort echo time cones magnetization transfer (UTE-Cones-MT) imaging and modeling with histological correlation. J Magn Reson Imaging 2018;48:160–168. [PubMed: 29219218]
93. Jerban S, Ma Y, Wan L, et al. Collagen proton fraction from ultrashort echo time magnetization transfer (UTE-MT) MRI modeling correlates significantly with cortical bone porosity measured with micro computed tomography (μCT). NMR Biomed 2018;32:e4045. [PubMed: 30549338]
94. Jerban S, Ma YJ, Nazaran A, et al. Detecting stress injury (fatigue fracture) in fibular cortical bone using quantitative ultrashort echo time-magnetization transfer (UTE-MT): an ex vivo study. NMR Biomed 2018;31:e3994. [PubMed: 30059184]
95. Xue Y, Ma Y, Wu M, et al. Quantitative 3D ultrashort echo time magnetization transfer (3D UTE-MT) imaging for evaluation of knee cartilage degeneration in vivo. J Magn Reason Imaging 2021;54:1294–1302.
96. Zhang X, Ma Y, Wei Z, et al. Macromolecular fraction (MMF) from 3D ultrashort echo time Cones magnetization transfer (3D UTE-Cones-MT) imaging predicts meniscal degeneration and knee osteoarthritis. Osteoarthritis Cartilage 2021;29:1173–1180. [PubMed: 33882334]
97. Wang Y, Liu T. Quantitative susceptibility mapping (QSM): Decoding MRI data for a tissue magnetic biomarker. Magn Reson Med 2015;73:82–101. [PubMed: 25044035]
98. Dimov AV, Liu Z, Spincemaille P, Prince MR, Du J, Wang Y. Bone quantitative susceptibility mapping using a chemical species-specific R2* signal model with ultrashort and conventional echo data. Magn Reson Med 2018;79:121–128. [PubMed: 28261863]
99. Jang H, von Drygalski A, Wong J, et al. Ultrashort Echo Time Quantitative Susceptibility Mapping (UTE-QSM) for Detection of Hemosiderin Deposition in Hemophilic Arthropathy: a Feasibility Study. Magn Reson Med 2020;84:3246–3255. [PubMed: 32662904]
100. Jang H, Lu X, Searleman A, et al. True phase quantitative susceptibility mapping using continuous single point imaging: a feasibility study. Magn Reson Med 2019;81:1907–1914. [PubMed: 30325058]

101. Lu X, Ma Y, Chang EY, et al. Simultaneous quantitative susceptibility mapping (QSM) and R2* for high iron concentration quantification with 3D ultrashort echo time sequences: An echo dependence study. Magn Reson Med 2018;79:2315–2322. [PubMed: 29314215]
102. Lu X, Jang H, Ma Y, Chang EY, Du J. Ultrashort Echo Time Quantitative Susceptibility Mapping (UTE-QSM) of Highly Concentrated Magnetic Nanoparticles: a Comparison Study about Different Sampling Strategies. Molecules 2019;24:1143.
103. Jerban S, Lu X, Jang H, et al. Significant correlations between human cortical bone mineral density and quantitative susceptibility mapping (QSM) obtained with 3D Cones ultrashort echo time magnetic resonance imaging (UTE-MRI). Magn Reson Imaging 2019;62:104–110. [PubMed: 31247253]
104. Nissi MS, Lehto LJ, Corum CA, et al. Measurement of T_1 relaxation time of osteochondral specimens using VFA-SWIFT. Magn Reson Med 2015;74:175–184. [PubMed: 25111731]
105. Wiesinger F, Menini A, Solana AB. Looping Star. Magn Reason Med 2019;81:57–68.
106. Larson PE, Han M, Krug R, et al. Ul Ultrashort echo time and zero echo time MRI at 7T. MAGMA 2016;29:359–370. [PubMed: 26702940]
107. Glover GH, Pauly JM. Projection reconstruction techniques for reduction of motion effects in MRI. Magn Reson Med 1992;28:275–289. [PubMed: 1461126]
108. Breighner RE, Endo Y, Konin GP, Gulotta LV, Koff MF, Potter HG. Technical Developments: Zero Echo Time Imaging of the Shoulder: Enhanced Osseous Detail by Using MR Imaging. Radiology 2018;286:960–966. [PubMed: 29117482]
109. de Mello R, Ma Y, Ashir A, Jerban S, Hoenecke H, Carl M, Du J, Chang EY. Three-Dimensional Zero Echo Time Magnetic Resonance Imaging Versus 3-Dimensional Computed Tomography for Glenoid Bone Assessment. Arthroscopy 2020;36:2391–2400. [PubMed: 32502712]
110. Foreman SC, Ashmeik W, Baal JD, et al. Patients with type 2 diabetes exhibit a more mineralized deep cartilage layer compared with nondiabetic controls: a pilot study. Cartilage 2019 Aug 27;1947603519870853.
111. Bydder M, Carl M, Bydder GM, Du J. MRI Chemical Shift Artifact Produced by Center-Out Radial Sampling of k-Space: A Potential Pitfall in Clinical Diagnosis. Quant Imaging Med Surg 2021;11:3677–3683. [PubMed: 34341741]
112. Peterfy CG, Guermazi A, Zaim S, et al. Whole-Organ Magnetic Resonance Imaging Score (WORMS) of the knee in osteoarthritis. Osteoarthritis Cartilage 2004;12:177–190. [PubMed: 14972335]
113. Byra M, Wu M, Zhang X, et al. Knee menisci segmentation and relaxometry of 3D ultrashort echo time cones MR imaging using attention U-Net with transfer learning. Magn Reson Med 2020;83:1109–1122. [PubMed: 31535731]
114. Xue Y, Jang H, Byra M, et al. Automated cartilage segmentation and quantification using 3D ultrashort echo time (UTE) Cones MR imaging with deep convolutional neural networks. Eur Radiol 2021;31:7653–7663. [PubMed: 33783571]
115. Kijowsky R, Liu F, Caliva F, Pedoia V. Deep learning for lesion detection, progression, and prediction of musculoskeletal disease. J Magn Reason Imaging 2020;52:1607–1619.

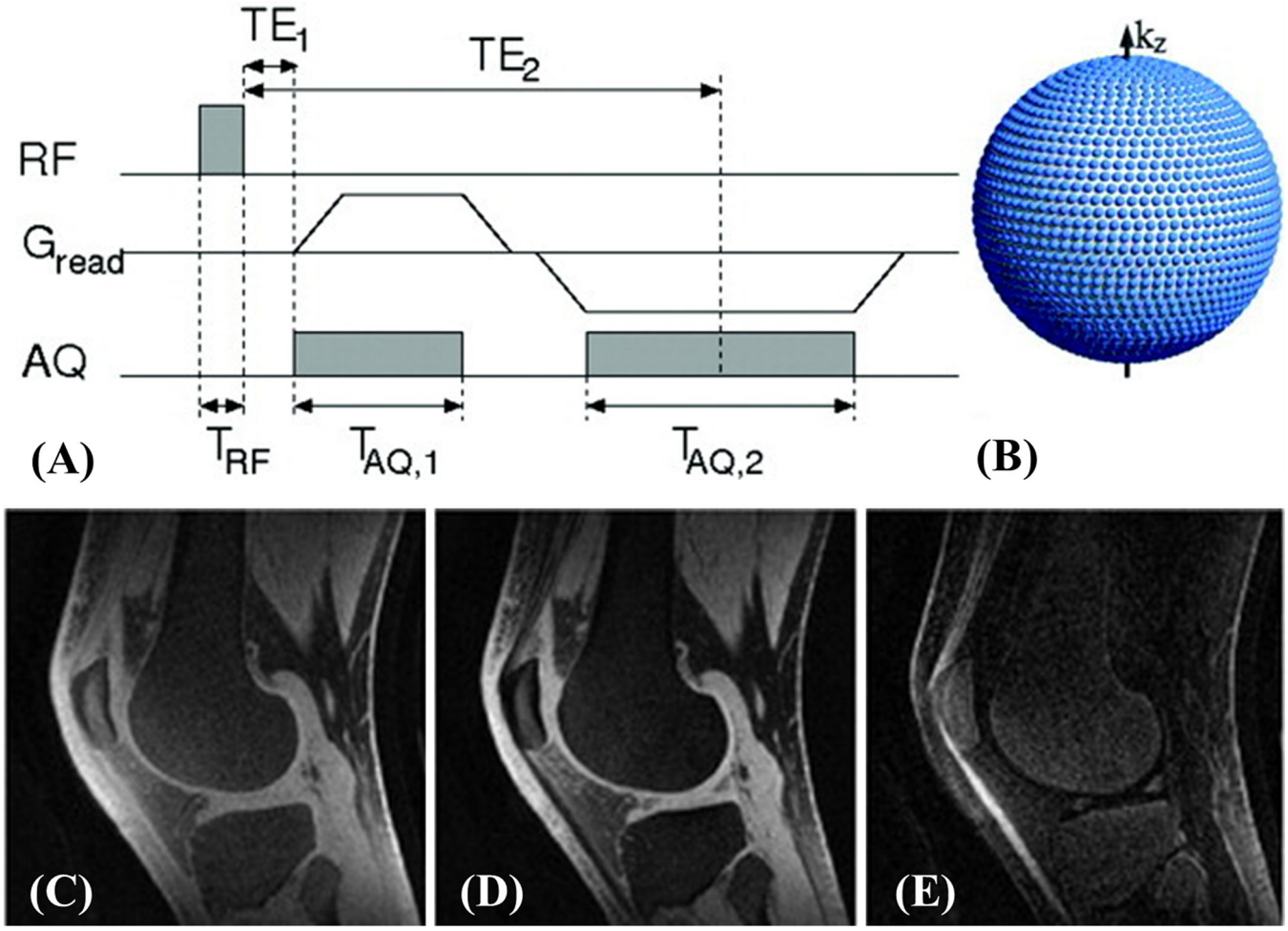

Figure 1.

The dual-echo 3D UTE sequence (A) and k-space trajectory (B), as well as 3D UTE data of the knee: FID image at TE=100μs with high signal from the patellar tendon and menisci (C), echo image acquired at TE=2.3ms (D), and difference image highlighting only short-T2 components (E). Modified from Ref. 6, with permission.

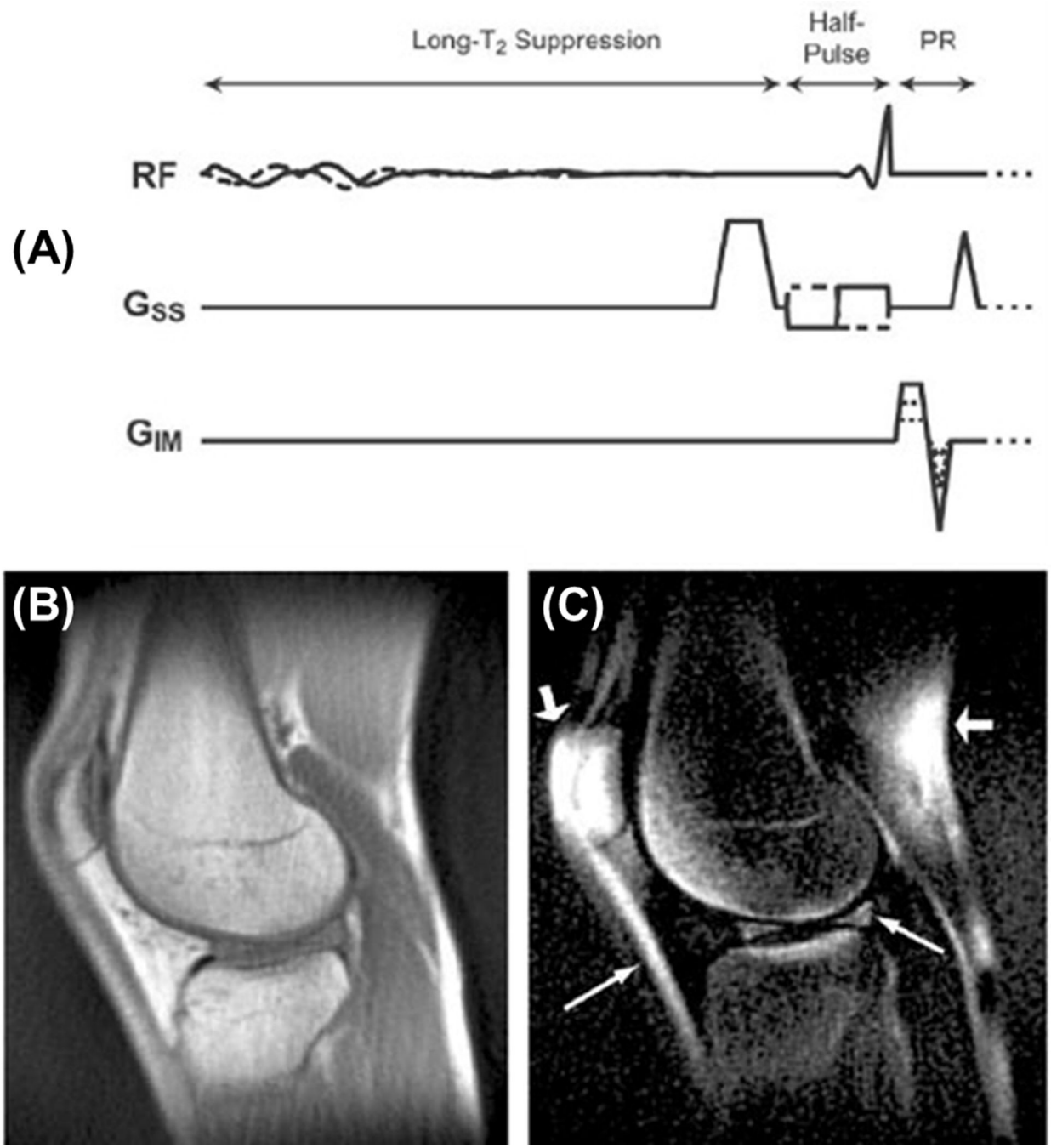

Figure 2.

The long-T2 suppressed 3D UTE sequence (A), and its application to the knee without suppression (B) and with a dual-band long-T2 suppression pulse (C). The suppression enhances the contrast of the short-T2 structures such as the patellar tendon and menisci (arrows). There is some fat suppression failure around the patella (short, thick arrows in C). Modified from Ref. 14, with permission.

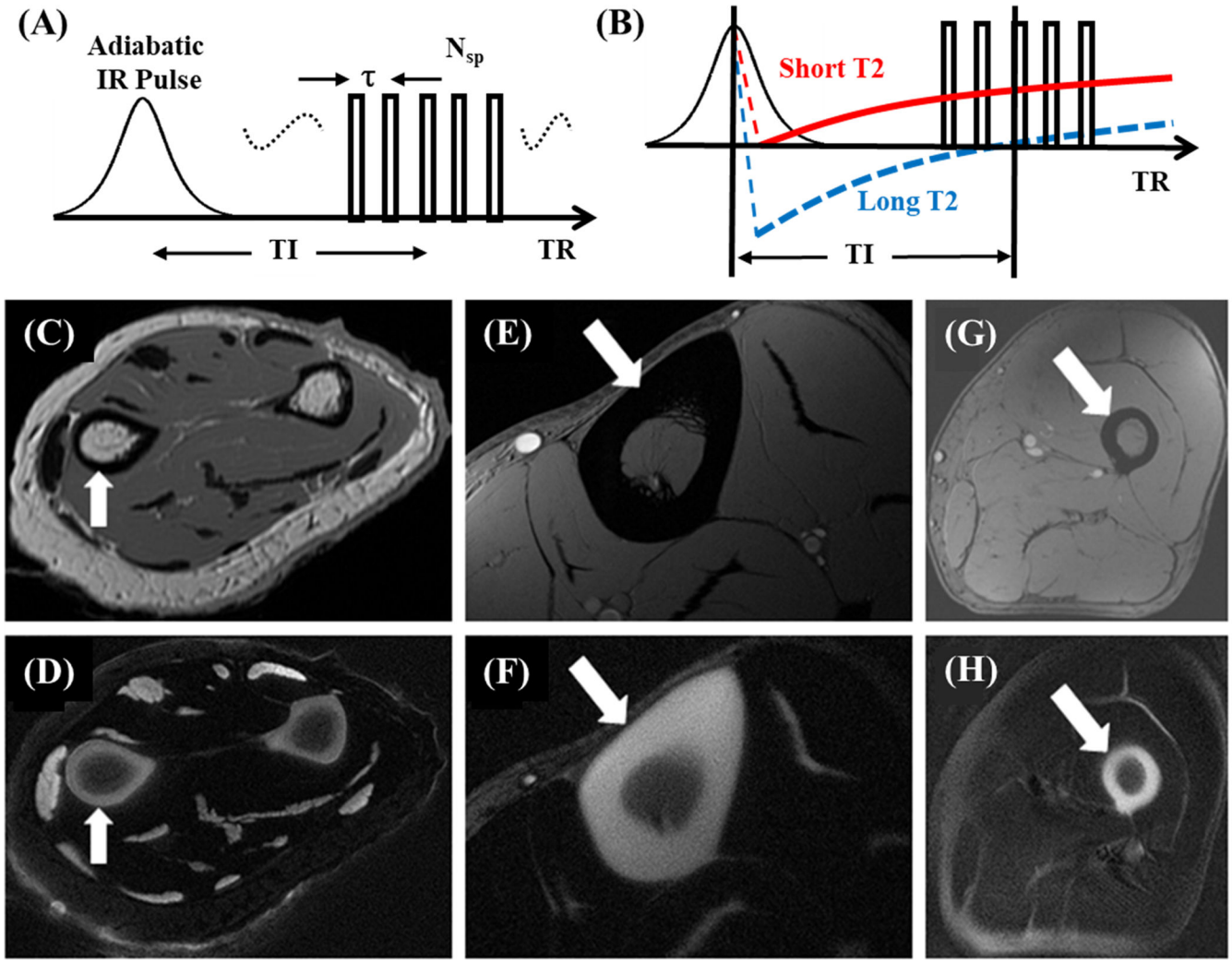

Figure 3.

The IR-UTE sequence employs a long adiabatic inversion pulse to invert and null long-T2 tissues, followed by multi-spoke UTE acquisition for high contrast imaging of short-T2 tissues (A, B). IR-UTE and conventional clinical MR imaging of cortical bone at various sites: forearm with FSE (C) and IR-UTE (D); tibia midshaft with gradient echo (E) and IR-UTE (F); and femoral midshaft with gradient echo (G) and IR- UTE (H). High resolution and contrast images of bone can be achieved in a clinical setting.

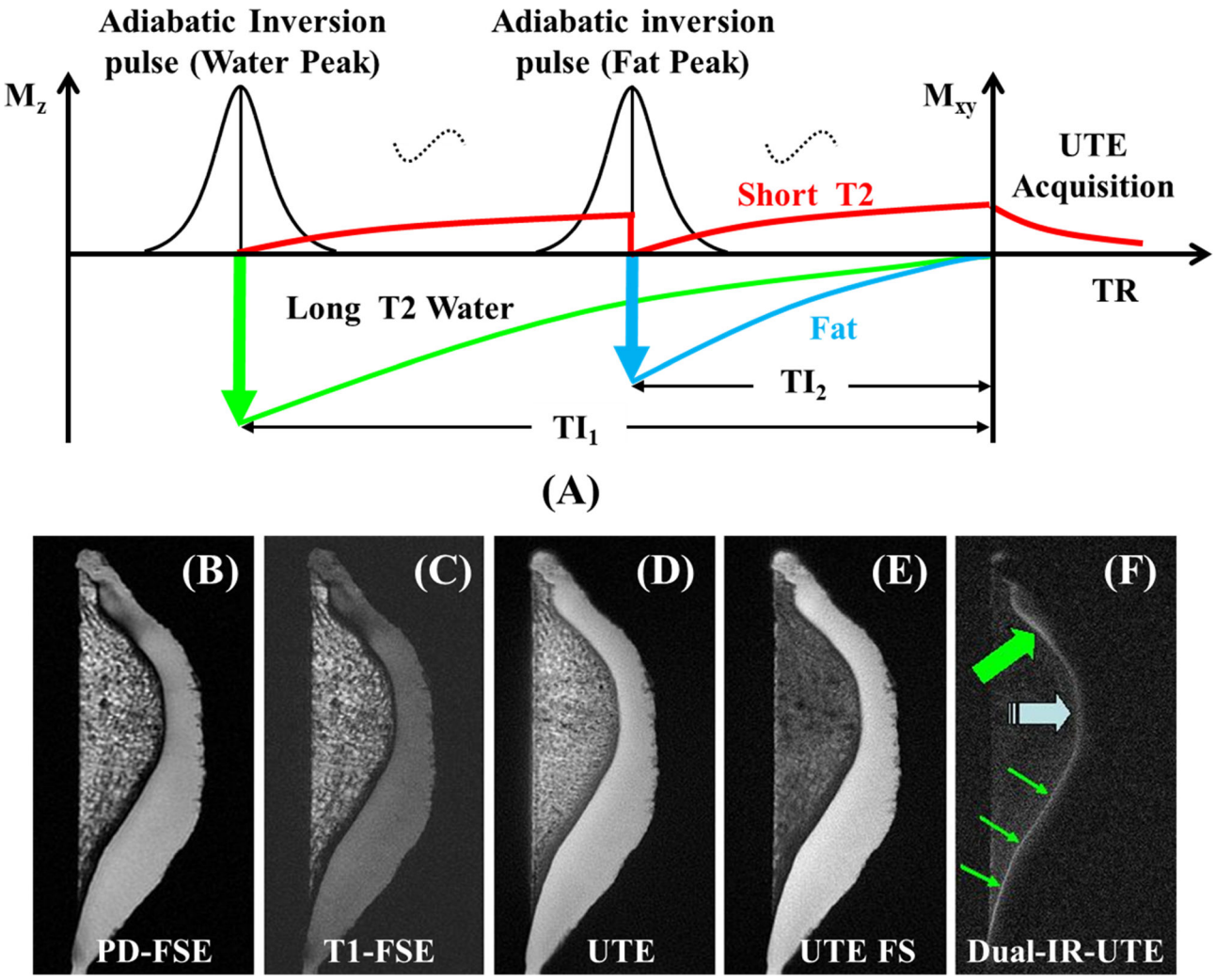

Figure 4.

The dual-IR-UTE sequence employs two long adiabatic inversion pulses to invert and null long-T2 water and fat, respectively, followed by UTE acquisition for high contrast imaging of short-T2 tissues (A). Its efficacy is demonstrated via imaging of a patella using PD-FSE (B), T1-FSE (C), regular UTE (D), UTE with fat saturation (E), and dual-IR-UTE sequences (F). The dual-IR-UTE sequence selectively suppresses signals from cartilage and marrow fat, creating excellent image contrast for the OCJ shown as a linear, well-defined area of high signal (thin arrows). Effacement and thickening (thick arrows) of the OCJ are also observed. Modified from Ref. 21, with permission.

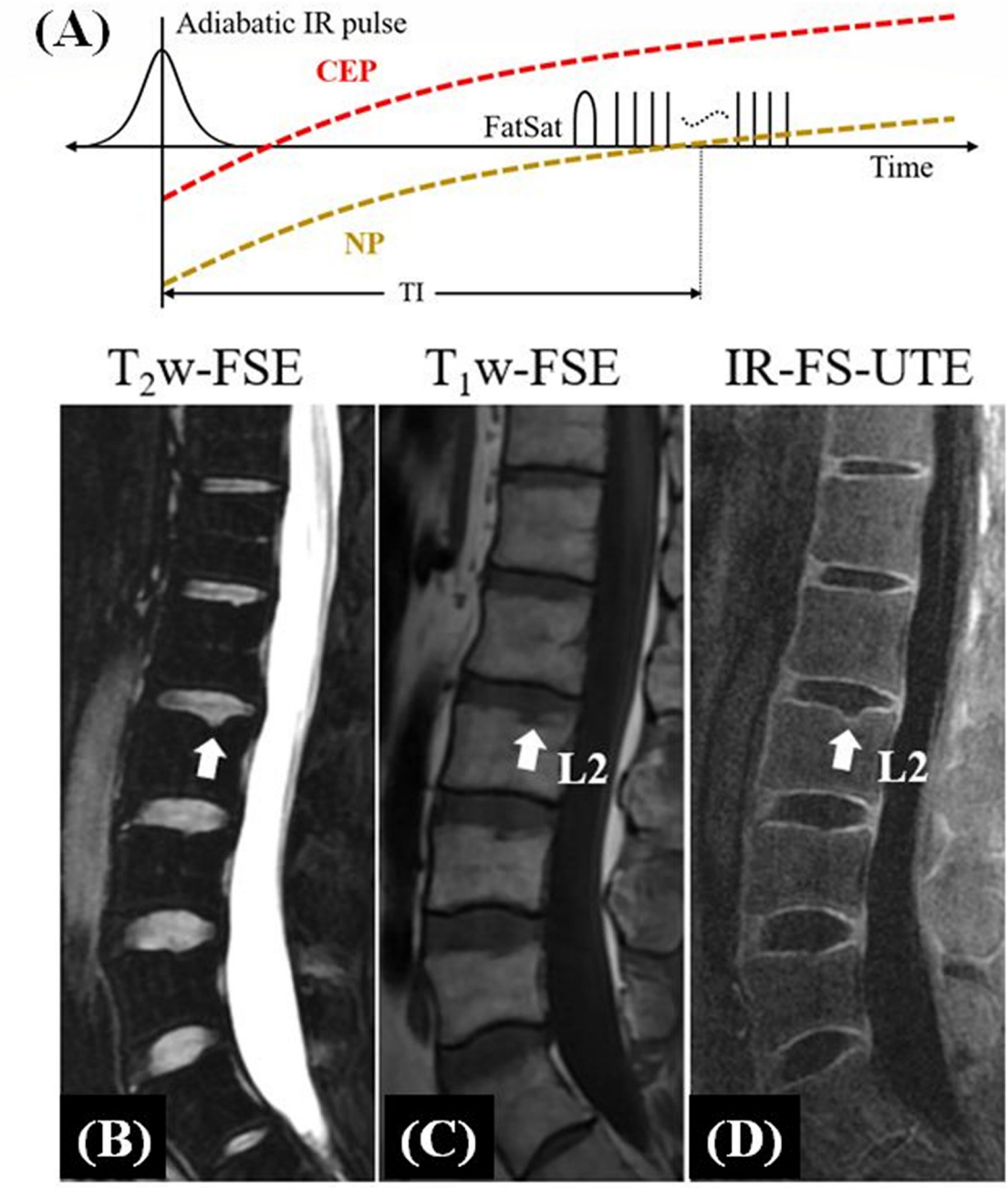

Figure 5.

The IR-FS-UTE sequence employs an adiabatic inversion pulse to invert long-T2 tissues, and a chemical shift-based fat saturation pulse to suppress fat signals, followed by multi-spoke UTE acquisition for high contrast imaging of short-T2 tissues (A). Its efficacy is demonstrated by sagittal T2-FSE (B), T1-FSE (C), and IR-FS-UTE (D) imaging of the spine of a 38-year-old male volunteer (T11-L5). The CEP is highlighted on the 3D IR-FS-UTE images (arrows in D) but cannot be seen on clinical sequences (B and C). Note the small and incipient Schmorl's node in the superior endplate of L2, with preserved CEP, that can

only be observed on the 3D IR-FS-UTE (arrows in B-D). Modified from Ref. 27, with permission.

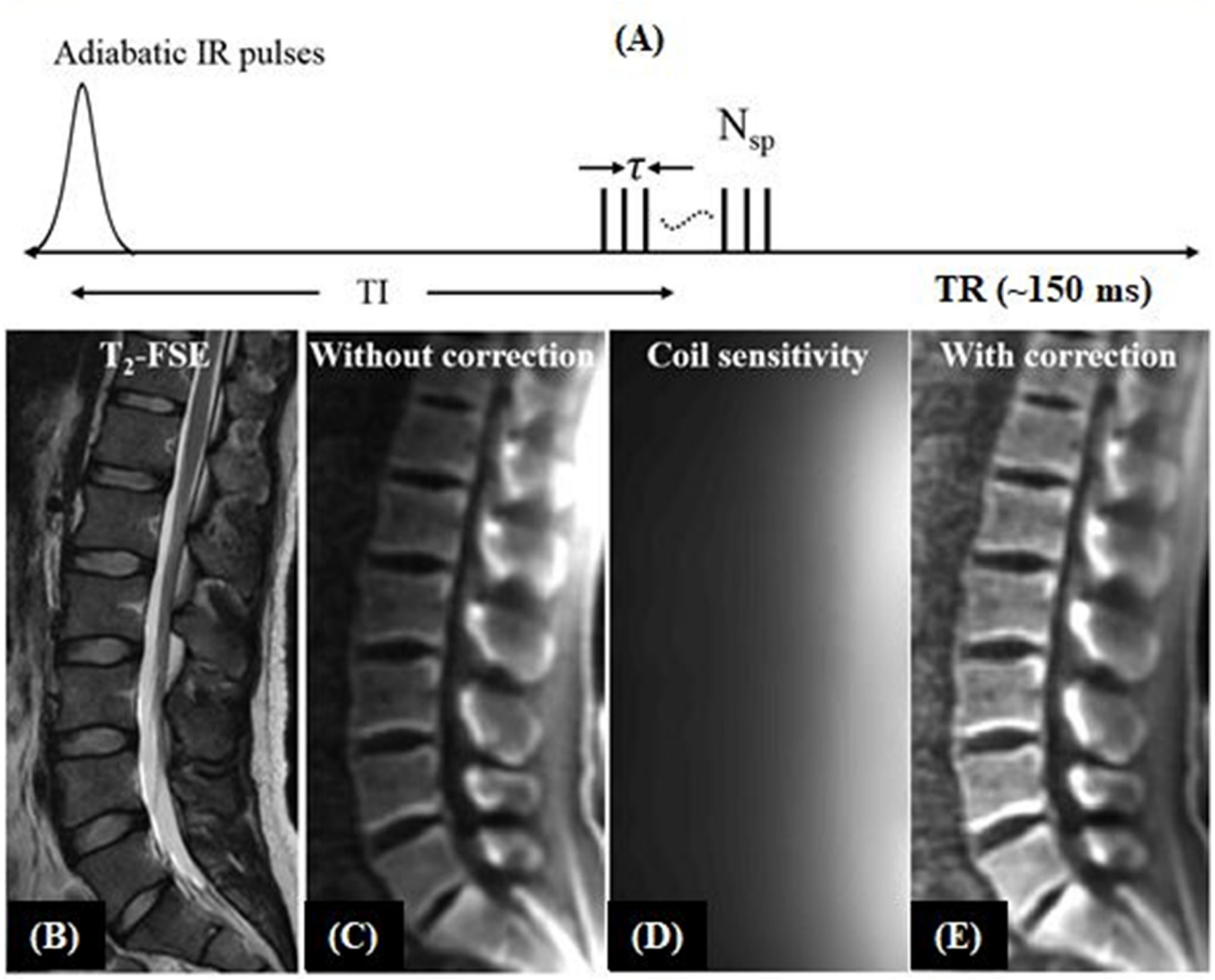

Figure 6.

The STAIR-UTE sequence employs a short TR and short TI for efficient suppression of long-T2 water and fat (A). Its efficacy is demonstrated by sagittal T2-FSE (B), and STAIR-UTE (C-E) imaging of the lumber spine of a 31-year-old volunteer. The long-T2 muscle and fat are bright in the clinical T2-FSE image (B). The original 3D STAIR-UTE image (C) shows non-uniform signal intensity distribution due to the inhomogeneous coil sensitivity (D) of the spine coil. After coil sensitivity correction, the image demonstrates a more uniform signal intensity distribution (E). Modified from Ref. 28, with permission.

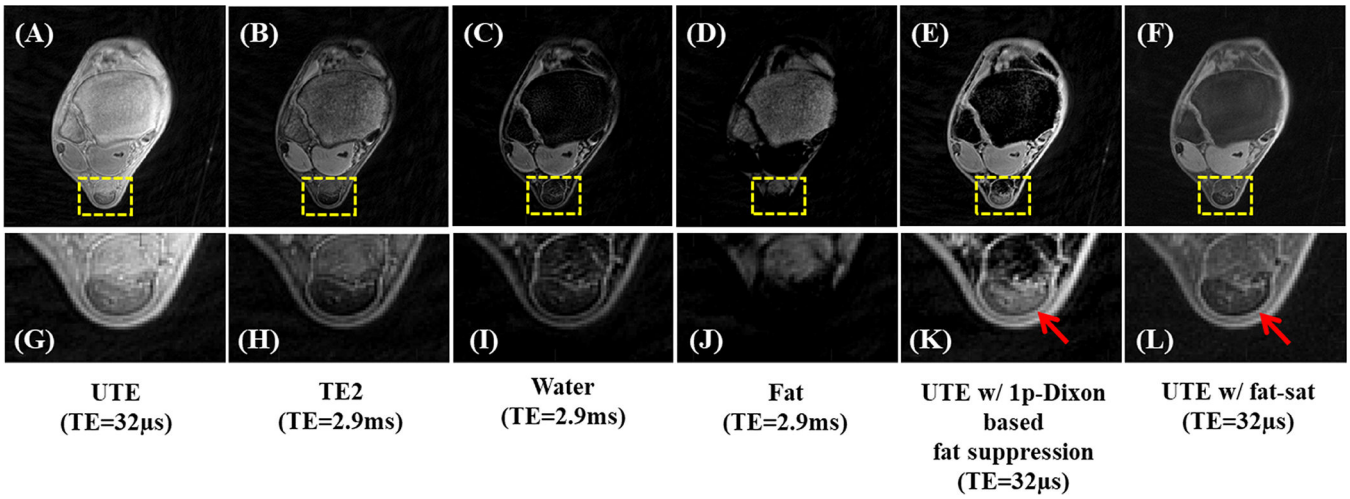

Figure 7.

The 1p-Dixon-based fat suppression for ankle imaging: the UTE image (A), the second echo (B), the estimated water image (C) and fat image (D), the UTE image with the 1p-Dixon fat suppression (E), the UTE image with chemical shift-based fat saturation (F), and the corresponding zoomed-in images (G-L). As indicated by red arrows in (K,L), the fat saturation pulse affects signals from the Achilles tendon, where signals in (F,L) appear much lower than UTE signals without fat saturation in (A,G). Meanwhile, the fat-suppressed UTE image with the 1p-Dixon approach in (E,K) shows similar signal intensities as the original UTE image in (A,G). Modified from Ref. 36, with permission.

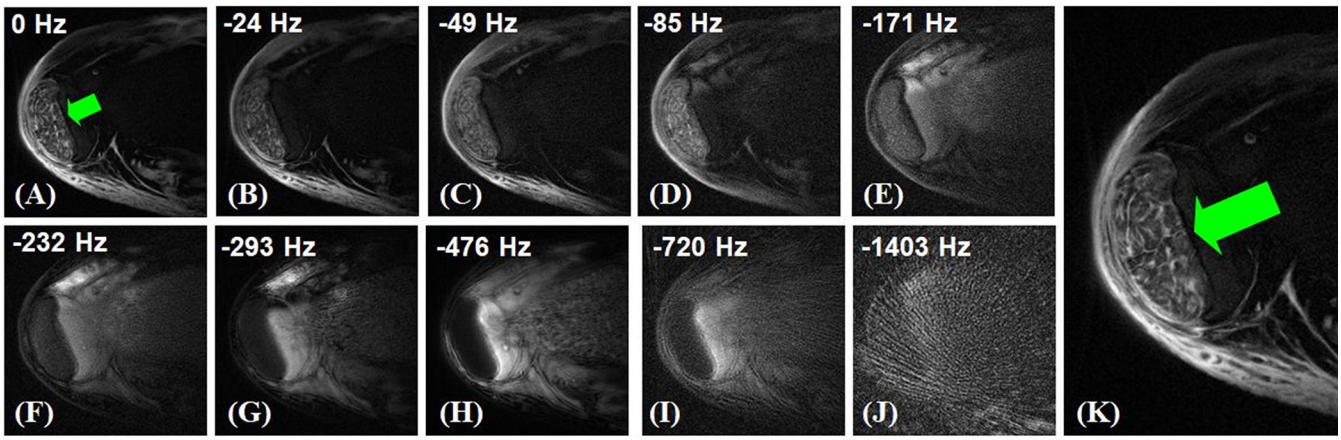

Figure 8.

Selected UTESI images of the tensile portion of the Achilles tendon at different frequencies of 0Hz (A), −24Hz (B), −49Hz (C), −85Hz (D), −171Hz (E), −232Hz (F), −293Hz (G), −476Hz (H), −720Hz (I), −1403Hz (J), and zoomed water peak at 0Hz (K). UTESI allows robust fat/water separation with undersampling streaks shifted to high spectral frequencies, providing excellent depiction of the fascicles and endotendon (K).

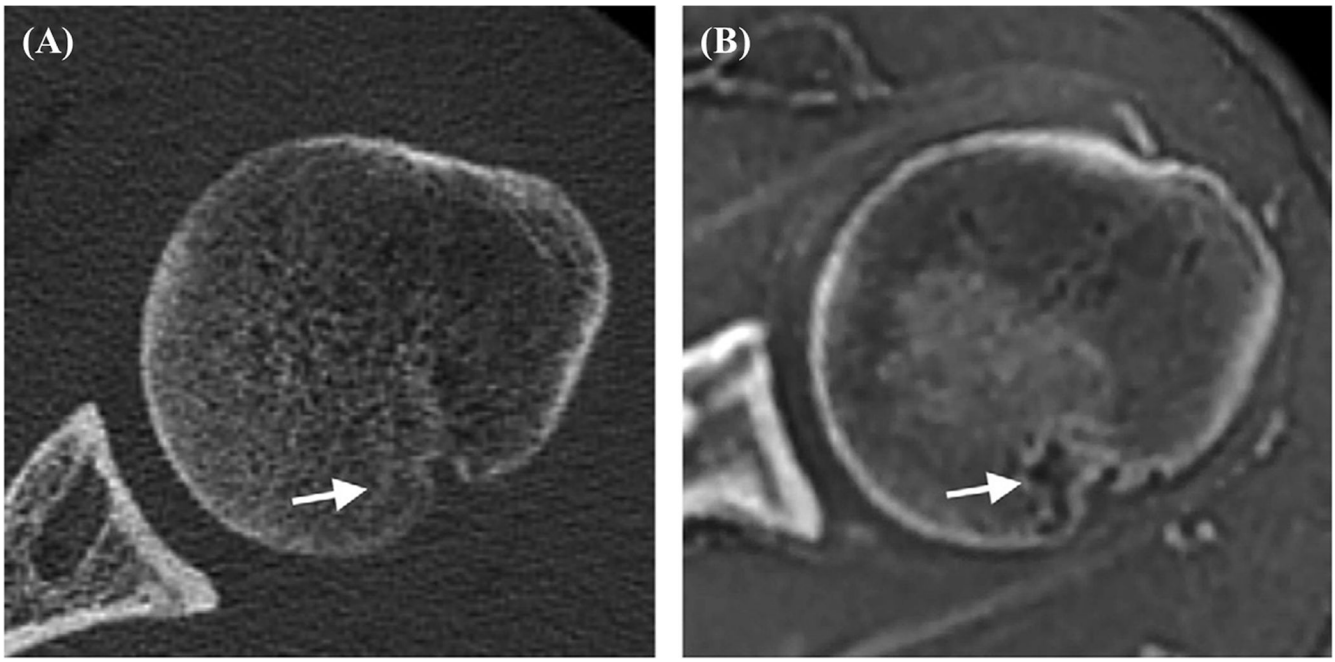

Figure 9.

The 3D UTE sequence with a single TR can be used for T1 measurement with the variable flip angle (VFA) method (A). The 3D UTE actual flip angle imaging (AFI) sequence employs a pair of interleaved TRs for accurate B1 mapping (B) which, when combined with the VFA method, provides accurate T1 measurements. Representative T1 fitting results for various knee joint tissues from a 35-year-old volunteer using the 3D UTE-AFI-VFA method: the measured T1 values are 832±18ms for meniscus (C, G), 779±7ms for quadriceps tendon (D,H), 637±16ms for patellar tendon (E,I), 870±13ms for ACL (F,J), 819±17ms for PCL (G,K), 1133±40ms for cartilage (H,L), 386±2ms for marrow (I,M), and 1406±63ms for muscles (J,N). Modified from Ref. 56, with permission.

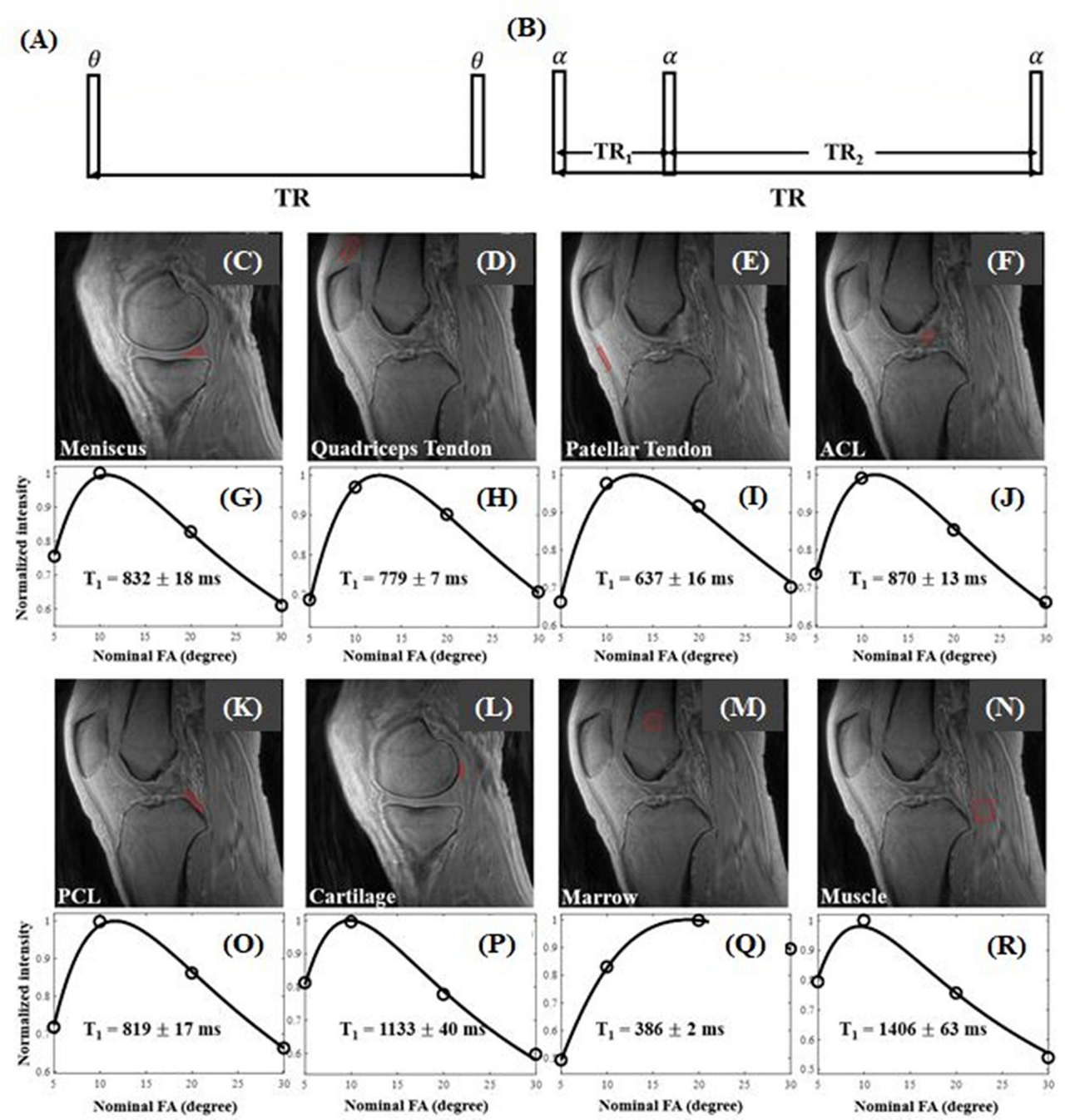

Figure 10.

UTE-T2* maps of the posterior medial menisci from (A) an uninjured control participant, (B) an ACL-reconstructed patient with an intact medial meniscus before surgery, and (C) the same patient 2years after ACL reconstruction (ACLR). (D) UTE-T2* mapping demonstrates subsurface meniscus matrix changes in the intact menisci of patients with ACL injuries. Before ACLR, UTE-T2* values in intact medial menisci of ACL-injured patients are 27% higher than those seen in uninjured controls (P=0.02). Over 2years after joint stabilization surgery, UTE-T2* values in intact menisci of ACL-reconstructed joints fall 17% (P=0.03)

to levels that do not differ from those of asymptomatic controls (P=0.7). As expected, UTE-T2* values in torn menisci before surgery are significantly higher (95%) than those of uninjured controls (P<0.01). Modified from Ref. 59, with permission.

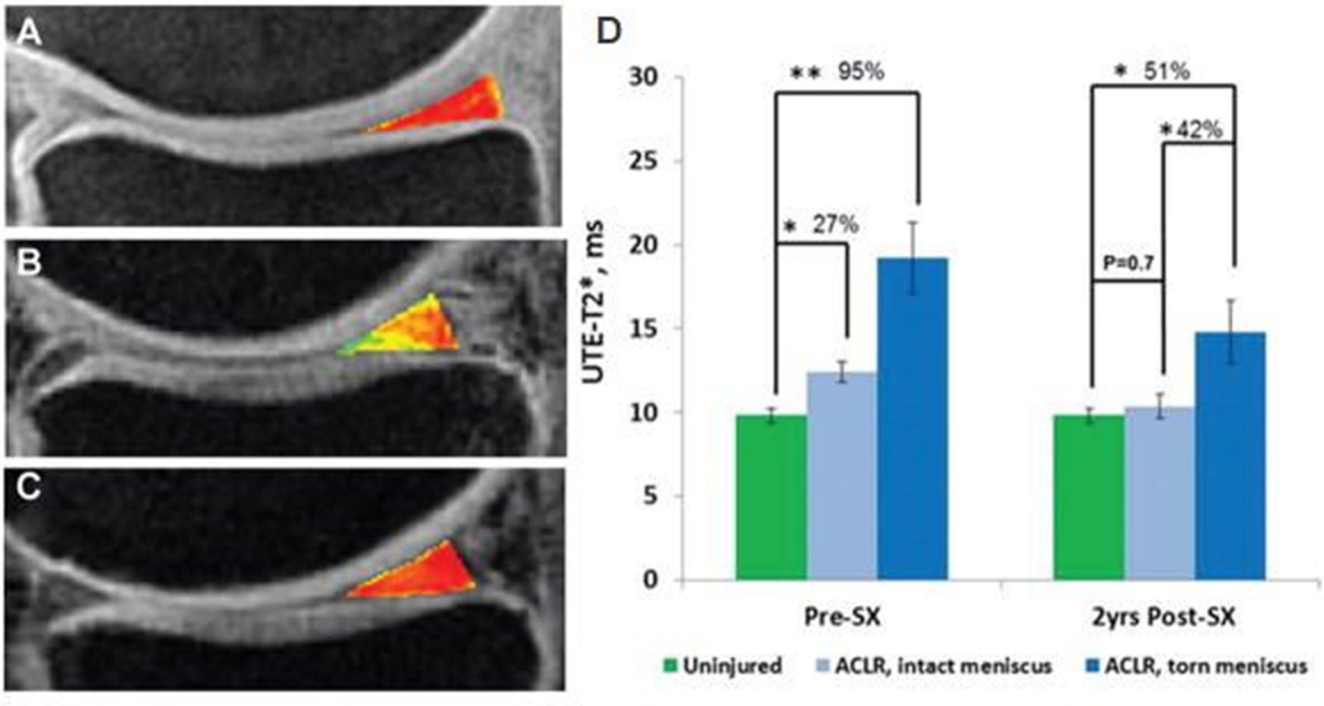

Figure 11.

The UTE-T1ρ sequence employs a spin-lock preparation pulse followed by single- or multi-spoke UTE data acquisition. The preparation pulse consists of a hard 90° pulse followed by a composite spin-lock pulse and another −90° hard pulse. The phase of the second half of the composite spin-lock pulse is shifted 180° from the first half to reduce artifacts caused by B1 inhomogeneity. Compared to conventional MAPSS imaging which shows little signal for the Achilles tendon (B) and limited signal for the meniscus (D) of a healthy young volunteer, the UTE-T1ρ imaging of the same volunteer shows much higher signal for both the Achilles tendon (C) and meniscus (E). Modified from Ref. 74, with permission.

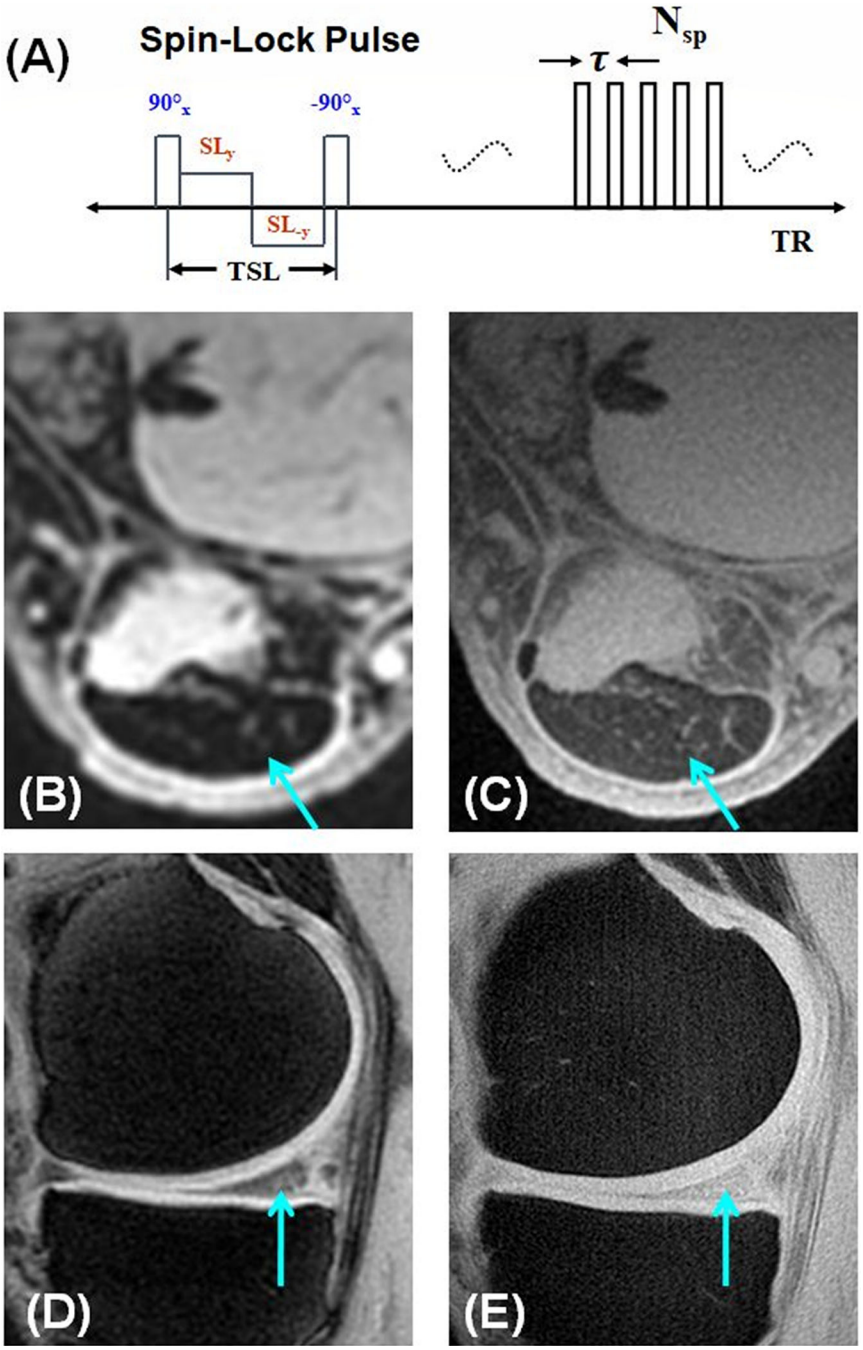

Figure 12.

The 3D UTE-AdiabT1ρ sequence employs a train of adiabatic IR pulse to generate T1ρ contrast, followed by multi-spoke 3D UTE data acquisition (A). Representative 3D UTE-AdiabT1ρ images of the knee joint of a 23-year-old volunteer with ROIs (red circles) and corresponding fitting curves of quadriceps tendon (B), PCL (C), meniscus (D), and patellar cartilage (E), as well as the corresponding exponential curve fitting showing UTE-AdiabT1ρ values of 13.7±1.0ms (F), 22.5±1.2ms (G), 21.5±1.1ms (H), and 43.5±5.9ms (I), respectively. Modified from Ref. 81, with permission.

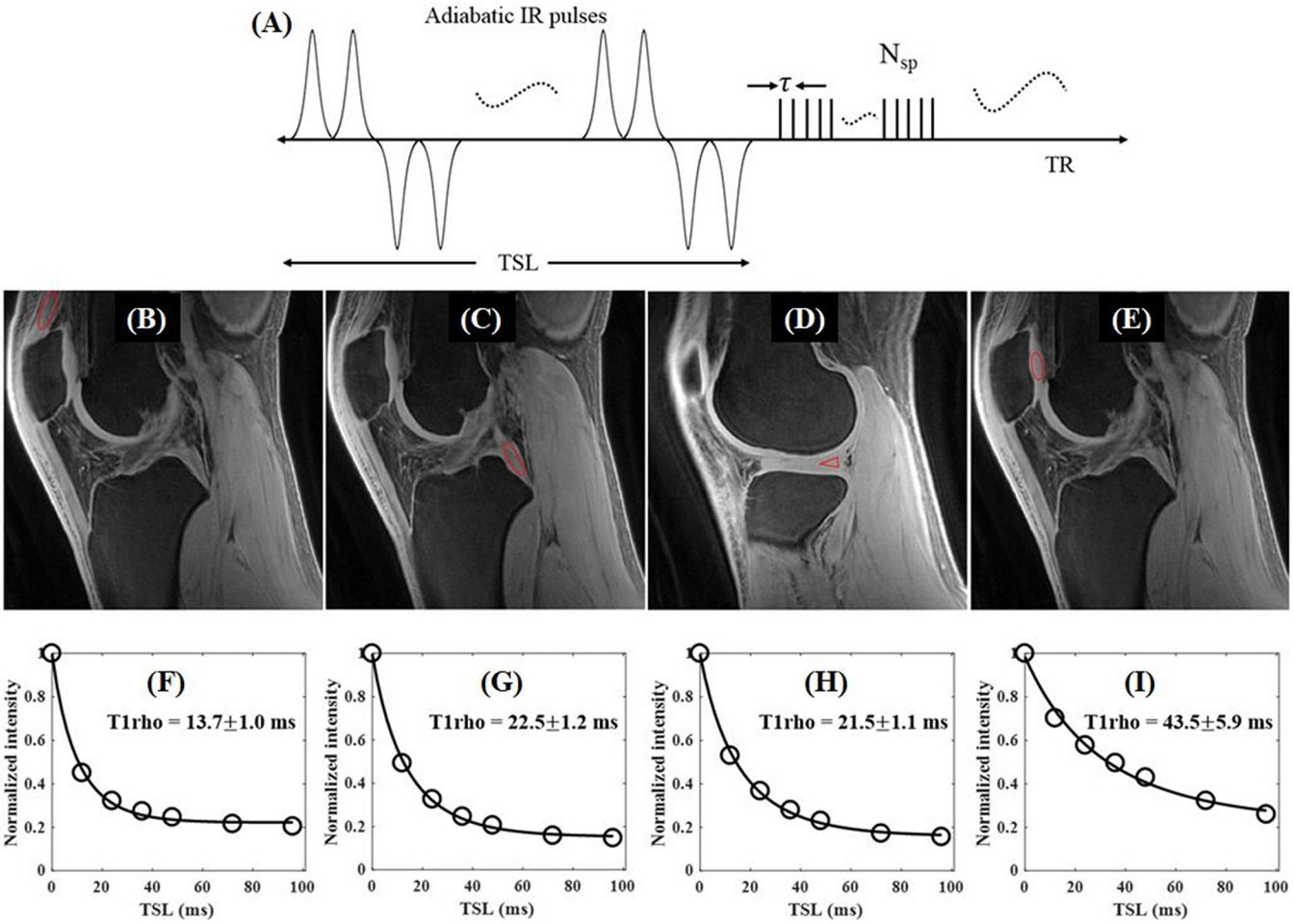

Figure 13.

The 3D UTE-MT sequence employs a Fermi pulse for MT preparation followed by UTE acquisition with a short rectangular pulse for signal excitation and a 3D Cones trajectory to allow time-efficient sampling with a minimal TE of 32μs (A). Multiple spokes (N_{sp}) are sampled after each MT preparation to speed-up data acquisition (by a factor of N_{sp}) (B). Selected 3D UTE-MT images of a bovine bone sample acquired with an MT power of 300° and five frequency offsets of 2kHz (C), 5kHz (D), 10kHz (E), 20kHz (F), and 50kHz (G), as well as an MT power of 1100° and five frequency offsets of 2kHz (H), 5kHz (I), 10kHz (J), 20kHz (K), and 50kHz (L). Excellent two-pool fitting is achieved with the RP model (M). Selected mapping of macromolecular proton fraction f (N), $T2_m$ (O), RM_{0m} (P), and R_{1w} (Q) are also displayed. Modified from Ref. 89, with permission.

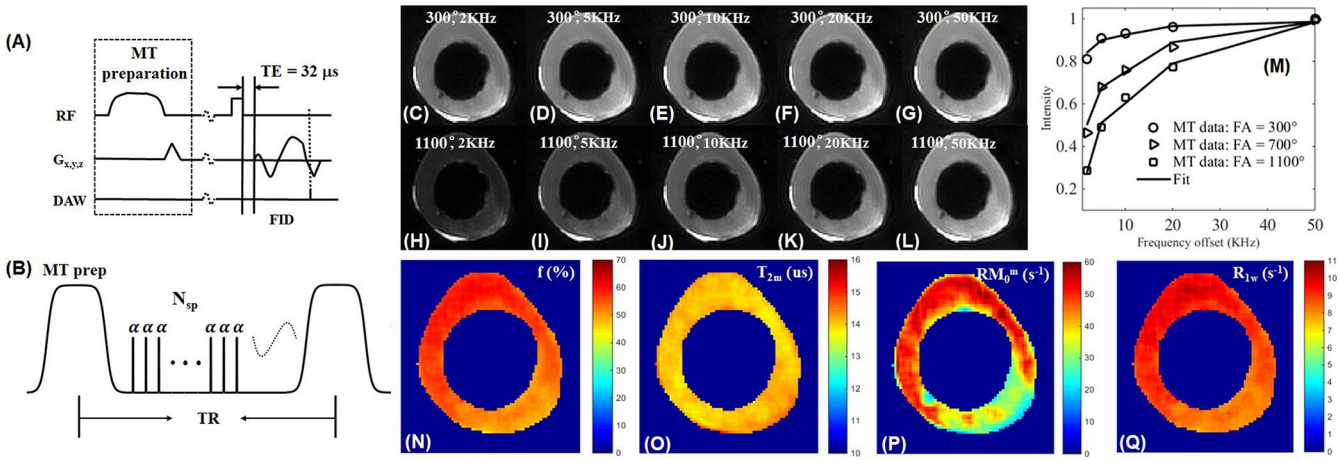

Figure 14.

Histology with synovial tissues (Tissue A and Tissue B) from a 28-year-old hemophilia patient who subsequently underwent TKA. Susceptibility map estimated in two representative slices (A and C) and the corresponding histological images (B and D). Blue dots in B and D exhibit iron (black and blue arrows). The measured susceptibility is 4.5±1.8ppm for Tissue A and 2.7±1.1ppm for Tissue B, which agrees with the observation that Tissue A shows denser iron than Tissue B in histology. Modified from Ref. 99, with permission.

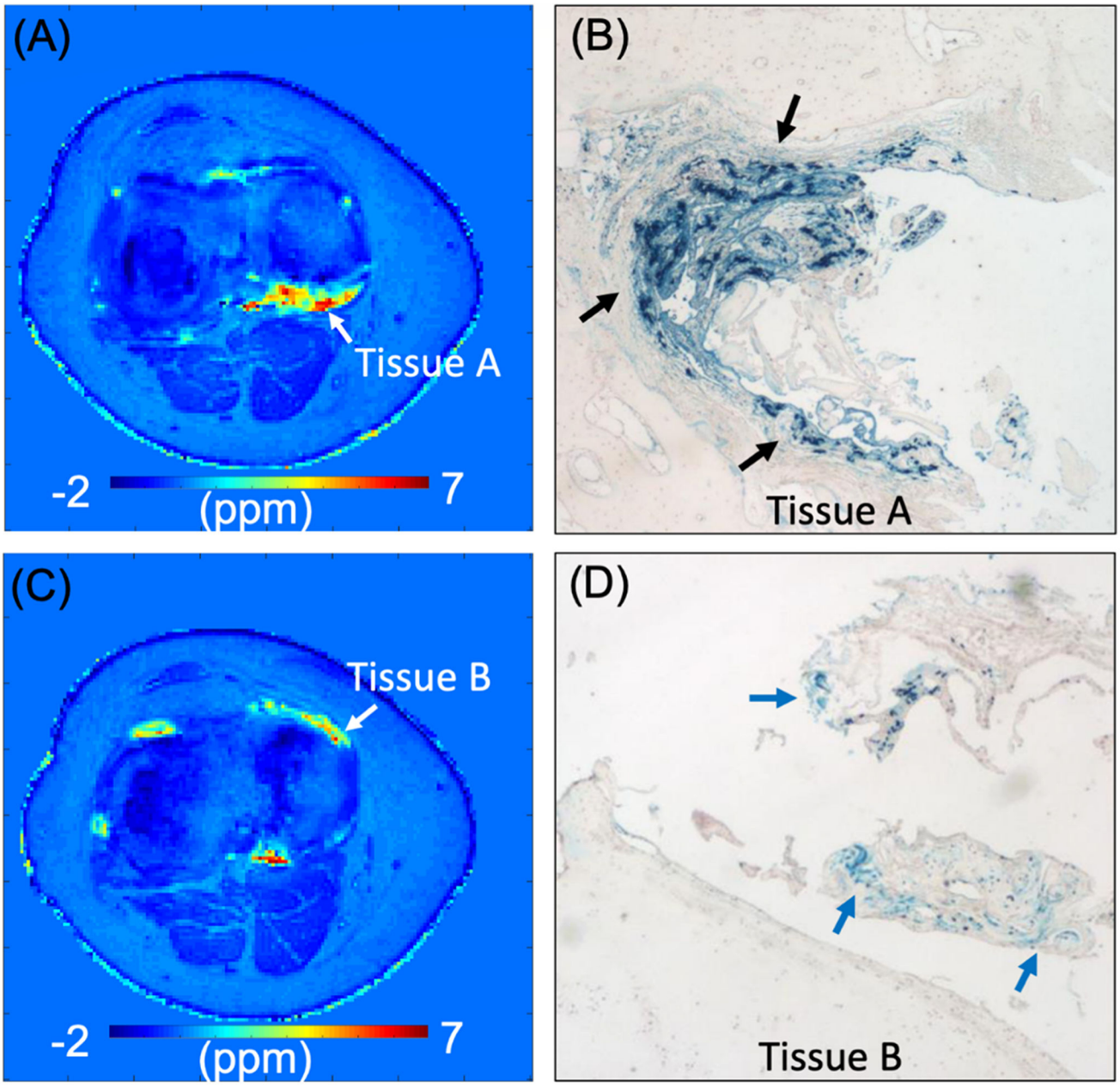

Figure 15.

UTE imaging of the human forearm as well as AIR mapping of bound water and DAFP mapping of pore water in tibial midshaft in the axial (1st row) and coronal (2nd row) planes. Modified from Ref. 51, with permission.

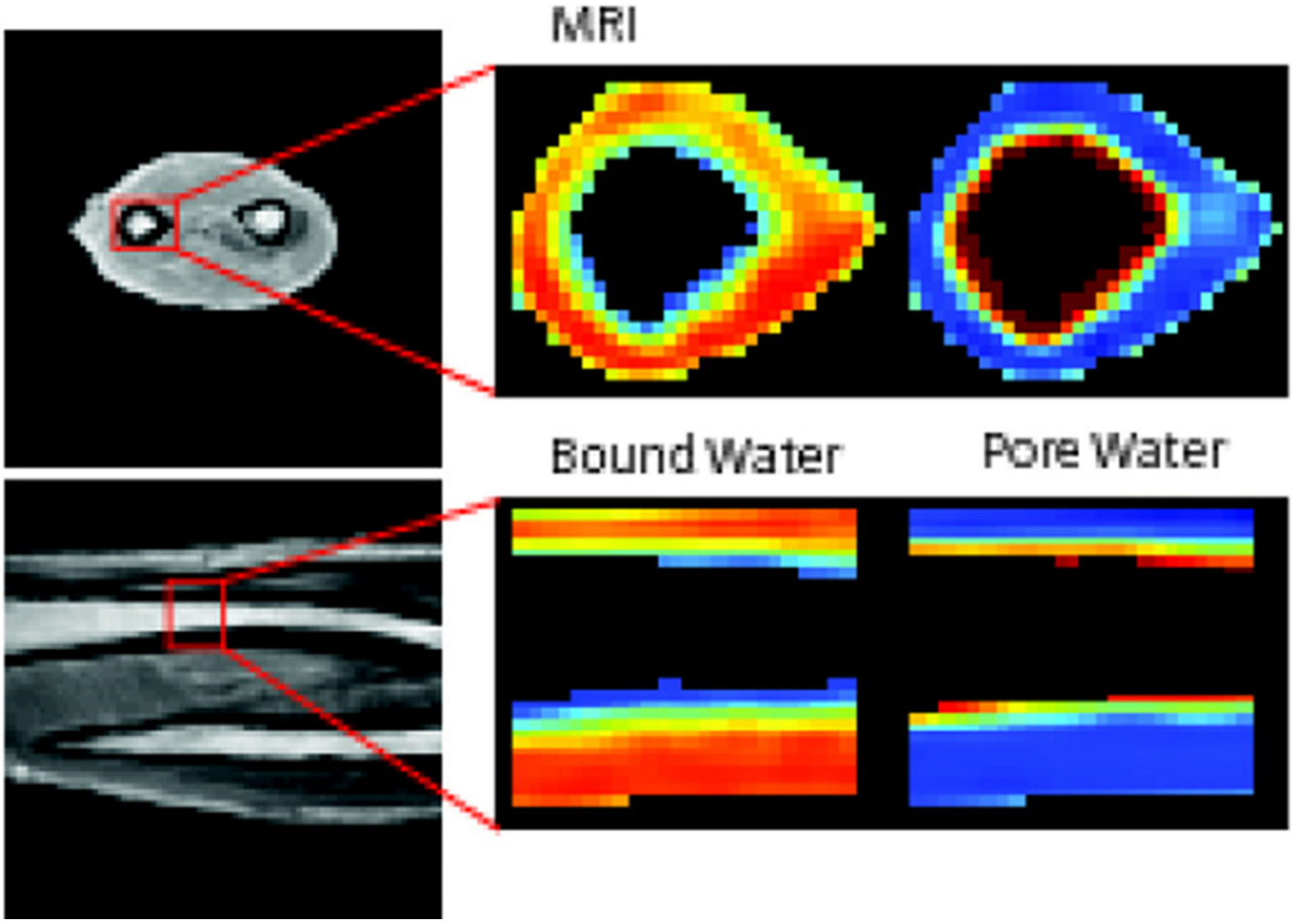

Figure 16.

Coregistered axial (A) CT and (B) ZTE MR images of the same humeral head in similar image planes in an 18-year-old man. An enthesopathic cyst manifests as hypointensity in the ZTE image (arrow in B). Arrow in (A) indicates the same location where the cyst is occult. The glenoid appears different because postures differed at acquisition of both images. Modified from Ref. 108, with permission.